PRECISE MONITORING OF HORIZONTAL DISPLACEMENT OF LARGE-SCALE STRUCTURES USING LOW-COST DUAL FREQUENCY GNSS RECEIVERS

A. M. Lapadat[1]

[1] MSc student GRS department, faculty of Civil Engineering and Geosciences, TU Delft, the Netherlands
a.m.lapadat@student.tudelft.nl

For the course CIE5050-09 Additional Research Project suppervised by Dr. ir. C. C. J. M. (Christian) Tiberius – Geoscience and Remote Sensing Department and Dr. M. Veljkovic – Engineering Structures Department.

KEY WORDS: Low-cost GNSS, Structural Health Monitoring, Multipath, Wind-induced Deformations, Sidereal Day Repeatability of Satellite Geometry

ABSTRACT:

Under urban sprawl the trend of new established complex structures has rapidly increased. In this context maintenance plays a major role and monitoring of such structures represents a first important step in combating disasters. Over the last years low-cost Global Navigation Satellite System (GNSS) equipment has faced rapid and important development opening a new door to reliable and high accurate positioning applications such as structural health monitoring.
This study presents a methodology for gathering, processing and analysing 1 Hz dual frequency GNSS data acquired by a network of newly released low-cost dual frequency GNSS receivers installed on a 90 metres tall steel-concrete structure in order to sense possible wind-induced displacements. At the same time, it represents one of the first studies testing the positioning capabilities of low-cost dual frequency GNSS equipment for monitoring large-scale building infrastructure.
The main tools exploited in this study are PPK relative positioning together with a multipath correction procedure based on GPS satellite constellation repeatability. In addition to these, several corrections are discussed and applied on the position estimates in order to achieve millimetre position accuracy, highly needed for sensing wind-induced displacements of large-scale structures. By artificially inducing some horizontal deformations it was found that the newly released low-cost dual frequency GNSS receiver can track centimetre order permanent deformations of tall buildings. In the context of not being able to identify strong statistical correlation between possible wind-induced deformations of the case study building and and wind data patterns, the study proves that wind-induced deflections of tall structures might be traceable only if they are larger than the magnitude of the carrier phase multipath effect that is “leaking” in the position estimates.

1. INTRODUCTION

In a world where skyscrapers, major bridges and dikes are nowadays necessity, safety should play an important role in the development and maintenance of these buildings. Within these processes reliable structural health monitoring of these objects plays an important role. Therefore, throughout their service life major structures should be thoroughly monitored in order to keep a close eye on their structural integrity and to know when to intervene with small or large maintenance steps for keeping them functional and safe. In addition to this, by monitoring large-scale structures after construction completion a better understanding of the used materials can be derived based on their response to natural disruptive factors such as wind storms, hurricanes, thunder storms or hail, making structural health monitoring a hot topic of nowadays structural engineering domain.
Until now traditional geodetic GNSS receiver and/or robotic total stations (RTS) were considered as the only high-accuracy static deformation monitoring alternatives. But with the release of inexpensive, robust and low energy consuming dual frequency GNSS receivers a door opened for affordable and accurate monitoring possibilities. This additional research project is proposing to evaluate the capabilities of a newly released low-cost dual frequency GNSS module to accurately determine wind-induced horizontal deformations of the 90 metres tall EWI (Faculty of Electrical Engineering, Mathematics and Computer Science) tower from Delft, the Netherlands. Therefore, the questions to be answered in this paper read:

“What is the accuracy potential offered by a low-cost dual frequency GNSS receiver? Is it sufficient for monitoring large-scale building deformations?”

The followed methodology, for finding an answer to the research questions and achieving the primary goal of this research, was to establish an optimal network emplacement of four GNSS receivers on the object of interest, let them acquire dual frequency pseudorange (code) and carrier phase observations over a long period of twenty days and then based on the later ones compute accurate relative horizontal coordinate time series via the Post Processed Kinematic (PPK) differential positioning technique. Having these observations, averaging over a wind-still period with little precipitation over which the structure stability could not be debated, was needed for defining the multipath signature over the wind-still period which could be further used for multipath correction and separation of possible wind-induced displacements during a stormy period over which potential building deflections could have happened.
As a side note, multipath (MP) is defined by Michael S. Braasch as ”the phenomenon whereby the signal from a satellite arrives at the receiver via multiple paths due to reflection and diffraction on nearby obstacles, distorting the received signal and causing errors in code and carrier phase measurements”

(Teunissen et al., 2017), and it is seen as one of the most disruptive effects which biases position time series encountered when using affordable GNSS antennas.
Last but not least, strong statistical cross correlation between the wind-induced displacement estimates and meteorological data sets containing wind speeds (WS) and wind directions (WD) was anticipated. This has been studied after translating and rotating the GNSS data set, from its European Terrestrial Reference System 1989 (ETRS89) regional coordinate system, together with the meteorological data set to a more suggestive local coordinate system with its coordinate axes defined across and along the case study building.
Since no significant statistical cross correlation could be found, several time periods when intense wind was blowing from favourable direction (South-West and/or North-East) were independently studied. During these periods any match between WS data sets and the rotated wind-induced displacement estimates was subjects of study. Even visual correlation between the identified horizontal position- and the meteorological patterns within the created plots was anticipated in order to be able to find an answer to the research questions.
The document describes the workflow involved in the sequence of operations that were conducted starting with the description of the case study building and its belonging deformation hypothesis in chapter 3, to data choice in chapter 4, followed by the theoretical aspects and followed procedure in order to: process the meteorological data sets and choose for relevant wind-still and windy days, process the GNSS data sets, correct for multipath and unwanted solutions and obtain accurate horizontal position estimate time series, translate and rotate the output time series from a regional coordinate system to a local coordinates system with favourable directions in order to better identify possible wind-induced displacements of the case study building in chapter 5. Right after, all results were analysed and presented in chapter 6. Finally, in order to give an answer to the phrased research questions the results were discussed and summarized. Recommendations for further research can to be found in chapter 7.

2. STATE OF THE ART/ LITERATURE REVIEW

This chapter is meant to give a brief summary of past conducted structural health monitoring studies based on **low-cost single frequency** and **high-end** GNSS technology with the aim of identifying the differences between both techniques in order to understand what one can offer with respect to the other. Conclusions can be used for anticipating the technological development of the new released low-cost dual frequency GNSS receivers. Since the later ones were newly introduced on the market few years ago, their positioning capabilities and limitations rise high interest among researchers and in the industry.
In addition to this, this chapter summarizes the **most common geodetic positioning techniques and equipment** that can be used for taking a decision on what technique to adopt for this study. Last but not least, a collection of the most important factors which are influencing the accuracy of the position estimates is listed, from which **multipath mitigation** is in detail discussed.

- **Low-cost single frequency GNSS technology**

  Over the past years structural health monitoring studies by means of GNSS technology were mostly based on different geodetic and geotechnical positioning techniques and equipment. Until now *low-cost* GNSS receivers were able to track satellite signals only on *one single frequency channel* and most of the research related to low-cost monitoring of structure deformations was done using this type of technology.
  An an example, A. Cina and M. Piras's solution was based on the **Virtual Station approach together with Network Real Time Kinematic (Network RTK) and relative positioning technique** using *low-cost single frequency* GNSS equipment (Cina , Piras, 2015). This technique uses a network of GNSS reference stations in order to virtually create a reference station close to the study area. In their paper A. Cina and M. Piras explained that by virtually creating a station one can understand that "the virtual station is not materialized, but its data are generated by the Network RTK in a known position defined by the user". This new virtual reference station is transmitting corrections to the remaining GNSS receivers which are operating as deformation monitoring rovers. By this the distance to the remaining rovers is kept small.
  Hence they used this technique to define virtual base stations very close to the point of interest in order to test the performance of a *low-cost* GNSS receiver and antenna system for landslide monitoring. For this they were using an artificial micrometric slide installed on top of a tall building for simulating landslides. Several tests were conducted where artificial horizontal and vertical displacements in the centimetre range were inferred in order to test the capabilities of the receiver to accurately capture three-dimensional movements. Throughout their research they obtained sub centimetre accuracy position estimates for acquisition times larger equal than 10 minutes and baselines smaller equal than 10 kilometres.

  Another example speaks about the possibility of **processing of carrier phase measurements using low-cost wireless sensor network technology in real time** (Heunecke, 2011). In comparison with the previous deformation sensing technique this one offers the possibility to return position solution in *near real time* since the data is broadcasted and processed to a central computer. Moreover, in case of major deformations, evacuation alarms can be conducted. For this a wireless sensor network, consisting of "*low-cost* GNSS receivers sensor field, master station or central computer, standard WLAN for communication, solar batteries with solar panels for power supply and proofed program tools", needs to be integrated.
  This technique should be taken into consideration in case of an extension of this research project as a master thesis subject.

- **High-end geodetic GNSS technology**

  In addition to low-cost single frequency GNSS equipment, *high-end geodetic* GNSS receivers were and still are preferred for structural health monitoring because of their operational integrity which comes with a higher price of the final cost and intense power consumption of the equipment.

Three different papers ((Lepadatu , Tiberius, 2014), (Takahashi et al., 2017), (Cina , Piras, 2015)) describe the use of this robust GNSS equipment in combination with **static relative positioning accompanied by short baseline post-processing in Post Processing Kinematic (PPK) mode**. This procedure involves to cover the structure of interest with fixed GNSS rovers and capture GNSS satellite signals in the form of code and carrier phase measurements which will be turned into every second position solutions with respect to a GNSS reference/ base station via PPK processing mode. The PPK mode is beneficial since it computes a position solution every second effectively outputting a time series of solutions in comparison to the Post Processing Static (PPS) mode which is outputting a final averaged position solution. This offers a good overview over possible position deviations within the time series of solutions, indicating structural deformations. However, this technique can only return solutions after some time since the position processing happens after conducting the measurements.
Y. Tamura et al. used this technique in order to prove that when using *high-end* GNSS receivers with a sampling rate of 10 Hz one can acquire building displacements induced by vibrations with frequencies larger equal than 2 Hz and amplitudes larger than 2 centimetres. He also proved that GNSS technology is better at retaining static wind-induced responses of buildings than the classic structural health monitoring measuring equipment, the accelerometer (Tamura et al., 2002).

- **Position error sources, Multipath**

Based on this literature review a collection of the most important factors -*multipath, instrument set-up, acquisition rate, base station-rover distance (baseline) and antenna choice*-, which are influencing the accuracy of the estimates were identified. Though, this research project was focusing more on the evaluation and mitigation of the *carrier phase multipath effect*.
In addition to the two GNSS technologies and positioning techniques listed above, some papers describe possible solutions for mitigating MP effect. One of these papers, written by H. van der Marel, describes a very useful property of the GPS satellite constellation which can be used for identifying MP signatures over daily position time series. As it will be in more detail presented in chapter 5, MP effect is highly dependent on: the height of the receiver antenna, the obstacles around it, the elevation and azimuth angle of the satellite. Since the GPS satellites have ground tracks on Earth with a repeat period of one sidereal day (00:00:00 - 23:56:04.0905 UTC)“ effects that manifest at a certain elevation angle and azimuth repeat with that period in a time series” (van der Marel, 2017). By relying on the sidereal day repeatability of the GPS satellite constellation one can use this property for any static GNSS receiver to identify its characteristic MP signature which can be further used for mitigating part of this vicious effect from any further daily position time series measured by the respective GNSS receiver.

Conclusions show that *low-cost single frequency* GNSS receivers could sense sub-centimetre displacements, when long enough position outputs were averaged out and tracking conditions were optimal. These results might be satisfactory for monitoring wind-induced deformations of most tall buildings. Moreover, *high-end geodetic* GNSS receivers were offering in addition higher sampling rates and dual frequency observations, facilitating the capture of high frequent sub-centimetre displacements of tall structures. Therefore, one can expect from **low-cost dual frequency GNSS receivers** to be an alternative to high-end geodetic equipment by offering an optimal balance between accuracy and cost-energy efficiency.
In order to get remarkable results almost all studies relayed on **PPK base station–rover correction transfer principle of relative positioning**. Therefore, this processing technique was preferred to be used when carrying out this research for sensing possible wind-induced displacements of the case study building.
Last but not least, a MP mitigation procedure for this study, relying on the sidereal day repeatability of the GPS satellite constellation, was identified.

3. CASE STUDY BUILDING & DEFORMATION HYPOTHESIS

The building of the Faculty of Electrical Engineering, Mathematics and Computer Science (EWI) is a 40,000 ton, 82.6 x 18 x 90 metre concrete-steel structure situated in Delft, the Netherlands. This complex structure is one of Delft’s landmark being one of the tallest buildings in the city. It was chosen as subject of study since it is known for its placement position which is predominantly influenced by South-West winds blowing from the North Sea. Its rectangular shape is capturing the wind from the top and amplifies it while pumping it to the ground. The choice of it as a case study structure relies on the building belonging to Delft’s University of Technology real estate making it more easier to get permission for installing GNSS equipment on top of it. On the other hand, since the South-East and North-West sides of the building consist of stiff concrete[1] the choice of this building as case study building might be not ideal for measuring possible wind-induced displacements within its structure.

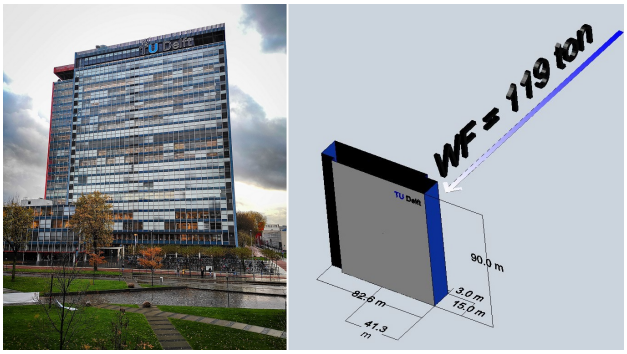

Figure 1. 3D visualization of the EWI building, its dimensions and the 119 ton horizontal wind force vector acting on the West façade. Picture of EWI’s East façade (left) and AutoCAD 3D drawing of East façade (rigth)

In order to set a hypothetical wind-induced deformation value of the top part of EWI building, the original document (van Bruggen et al., 1963) describing the structural calculations of the wind deformation on the glass façades of EWI was studied. Since this document describes structural design calculations the drawn hypothesis should be treated as a safe, possibly

[1] painted in blue in Figure 1.

largely exaggerated upper bound. Additional information of this building, such as the elasticity modulus (Ec) of the pillars situated at the flanks of this tower and of the metal beams in the in-between structure of 300,000 respectively 2100,000 $[\frac{kg}{cm^2}]$, was presented. In this document J. P. van Bruggen et al. were considering an extreme 85 $[\frac{kg}{m^2}]$ pressure wind vector, equivalent with a powerful 14 Beaufort windstorm, perpendicularly hitting the West side of the building. In addition, the storey floors were considered to be infinitely stiff meaning that the wind forces acting on the façades were transferred through them. It was also assumed that the ground floor of the building would remain horizontally unchanged under wind loads, acting as a cantilever.
By following the authors reasoning and calculations, this study was assuming an East inclination of approximately 1.3 centimetres of EWI's roof top under a 8 Beaufort wind gale (equivalent to a wind pressure of approximately 23 $[\frac{kg}{m^2}]$) blowing perpendicular on the West façade of EWI. In the next lines the structural computations, on behalf of which the previous value was obtained, are presented.

In the first step the wind pressure of 23 $[\frac{kg}{m^2}]$ was used for computing the wind load (WL) hitting on the West façade:

$$WL = 0.23 * (0.9 + 0.4) * (23 + 20 * 1.5) \cong 16 \ \frac{kg}{m^2} \quad (1)$$

Right after, one could compute the wind force (WF) as the wind load multiplied by the area of the influenced side of the building:

$$WF = WL * surf_{area} = 16 * 82.6 * 90 \cong 119 \ ton \quad (2)$$

This meant that the wind pressure of a 8 Beaufort wind gale was applying a 119 ton force in the middle (41.3 x 45 m) of the West façade of EWI (see Figure 1). In order to compute the moment of the wind force (M_0) at ground floor one was multiplying WF with the half height of the building[2]:

$$M_0 = WF * \frac{height}{2} = 119 * 45 = 5355 \ ton * m \quad (3)$$

In order to get to the final wind-induced displacement value (S) a set of considerations were taken into account:

- **Concrete walls displacement – Considering only the concrete side walls of the building (no steel construction, no rejuvenated bulkheads), where each side wall is formed out of five bulkheads, the deformation on the roof top was equal to S = 1.3 cm**

This resulted from first computing the reduced moment lines of each concrete bulkhead:

$$\begin{aligned} M_a = 0.0345 M_0, M_b = 0.0272 M_0, \\ M_c = 0.0201 M_0, M_d = 0.0277 M_0 \end{aligned} \quad (4)$$

The moment lines were used for determining the deflection at each bulkhead. Then one could compute[3] the total deflection (S) of the non-rejuvenated concrete bulkhead at 90 metres:

$$\begin{aligned} S = \frac{El_0 S * M_0}{Ec * y_0} = \frac{2102.7 * 5355}{3 * 10^6 * 267} \cong 1.4 \ cm \\ \frac{77.7 * 5355}{3 * 10^6 * 267} \cong 0.1 \ cm \text{ (rejuvenated bulkheads)} \end{aligned} \quad (5)$$

By subtracting the two values from equation set (5):

$$S = 1.3 \ cm \quad (6)$$

- **Concrete walls displacement after rejuvenating – When taking into account rejuvenate bulkheads**

$$\frac{4}{3 + 0.5} * 1 = 1.14 \ mm \cong 0.1 \ cm \quad (7)$$

$$S = (6) + (7) = 1.4 \ cm \quad (8)$$

- **Reduction of displacement by taking into account steel structure**[4]

$$\frac{0.135 * 5355}{6500} * 26.5 \cong 0.2 \ cm \quad (9)$$

$$S = (8) - (9) = 1.2 \ cm \quad (10)$$

- **Increase in deflection caused by excess weight of the building while inclining/ bulking**

Bulking is caused by the excess weight of the inclining top part of the building. To the current displacement a bulking factor ($V_{beton+steel}$) needed to be applied. This bulking factor was computed[5] based on the bulking factor of the concrete structure (takes into account on the total weight of the building of 40,000 ton) V_{beton} = 19.4.

$$\begin{aligned} V_{beton+steel} = \frac{(6) + (7)}{(10)} * V_{beton} \\ = \frac{1.4}{1.2} * 19.4 \cong 22.63 \end{aligned} \quad (11)$$

$$S = \frac{V_{beton+steel}}{V_{beton+steel} - 1} * (10) = \frac{22.63}{21.63} * 1.2 \cong 1.3 \ cm \quad (12)$$

This short chapter was meant to describe the case study building from the structural point of view and define some hypothetical values of wind-induced displacements of the building in order to get a feeling on the order of magnitude of the expected wind-induced deformation. It should be mentioned that the presented calculations are based on the original design document of the building but since this document was written before construction one cannot fully relay on the final result but can only take it as an indicative, likely over-estimated deformation value.

[2] for better understanding of equations 1, 2, 3 inspect page 1 of the original document (van Bruggen et al., 1963)

[3] for better understanding of equations 4, 5 inspect pages 2-3 of the original document (van Bruggen et al., 1963).

[4] for better understanding of equations 7, 9 inspect page 145 of the original document (van Bruggen et al., 1963)

[5] for better understanding of equations 11 inspect pages 144-145 of the original document (van Bruggen et al., 1963).

4. DATA COLLECTION

4.1 Data type

Two different types of data sets, GNSS and meteorological, were used in this research. Both were collected over twenty days from 12/11/2019 until 02/11/2019. Each of the data sets is described below in detail.

- **GNSS data set(s)**

Since the study was based on post-processed GNSS differential positioning (PPK) one needed two types of data sets collected by a GNSS base station and a third one collected from the network of u-blox ZED F9P GNSS rover modules installed, 1.7 kilometres away from the base station, on top of EWI.
The first needed GNSS data set was coming from the DLF1 base station of the Dutch Permanent GNSS Array (DPGA) which is consisting of "eighteen continuously operating GPS (and GLONASS) receivers in the Netherlands"[6]. DLF1 was installed on top of the Dutch Metrology Institute (NMI) from Delft in March 2011 and consists of a high-end geodetic Trimble NETR9 receiver and a Leica LEIAR25.R3 antenna (see Figure 2). More information about it and its operation status can be found at: `http://gnss1.tudelft.nl/dpga/station/Delft.html`.

Figure 2. DLF1 high-end Leica LEIAR25.R3 geodetic antenna installed on top of NMI building. Picture in pointing in West direction

For reaching the purpose of this research project, 15 minutes stacks of 1-second mixed observations (MO, containing GPS, GLONASS, GALILEO, BEIDOU, QZSS and SBAS observations) files were downloaded, decompressed and merged by using a self-written Matlab script, which is asking for the day of year of interest in order to establish a ftp connection with `http://gnss1.tudelft.nl/dpga/rinex/highrate/2019/` and form **24 hours 1-second MO files**. The same Matlab script is downloading and decompressing the second needed GNSS data set from the DLF1 base station as well, namely the **broadcast mixed navigation/ephemeris data set (MN)**. This data set contains the orbit, clock parameters and auxiliary data coming from the GNSS satellites ((Teunissen et al., 2017), p. 1213) and has the purpose of calculating the position of each satellite and gives additional information on their status.
The third needed GNSS data set was collected via a GNSS rover network consisting of four dual frequency low-cost GNSS modules. These modules were acquiring **rover GNSS observations** with a sampling rate of 10 Hz (every one tenth of a second). The GNSS data was logged on a Raspberry Pi Zero computer with a memory limit of 16 GB. Because of this memory limit over the period of study two data-logging interruptions were needed for collecting the data and emptying out the memory of the loggers. More information about the exact start-stop time spans are presented in Figure 3 and in the GNSS logsheets annexed at the end of this document.

Receiver Name	Start Date	UTC Start time [hh:mm]	Stop Date	UTC Stop time [hh:mm]	Obs.
EWI01 EWI02	12/11/2019	14:46	15/11/2019	14:10	EWI01 - metal struct. EWI02 - conc. tile +GP
	15/11/2019	14:48	25/11/2019	12:24	
	25/11/2019	12:44	02/12/2019	12:12	
EWI03 EWI04	12/11/2019	15:38	15/11/2019	14:51	EWI03 - conc. tile EWI04 - conc. tile +GP
	15/11/2019	15:01	25/11/2019	12:12	
	25/11/2019	12:31	02/12/2019	12:20	

Figure 3. Start-Stop time information of each rover receiver from the wind-displacement GNSS array on the EWI building

- **Meteorological data set(s)**

A meteorological data set spanning over the same period as the GNSS data sets was provided by Ing. Ron van Puffelen, member of the EWI/ Electronic Instrumentation Laboratory. Live broadcast of this type of data set can be found at: `http://weather.ei.tudelft.nl/WindSensor3.php`. This data set was acquired by a meteorological station mounted on top of EWI building and consists of every second wind speed (WS), wind direction (WD) and drop size precipitation (DS) observations. According to R. van Puffelen the EWI meteorological station data set is not recommended to be used for accurate meteorological predictions because of the unusual emplacement of the meteorological station on top of a tall tower, but for this study it best fits the research goal since wind information was captured as close as possible to the GNSS rovers.

A very important remark one needs to take into account is related to the time frames of the above presented data sets. GNSS data is aligned with the GPS Time (GPST), a continuous time scale measured by atomic clocks located at ground stations and onboard satellites. The origin of the GPST time scale is at 00:00:00 UTC of January 5th to 6th 1980[7]. GPST is not corrected to match the rotation of the Earth, so it does not contain leap seconds or other corrections that are periodically added to UTC [8].

[6] `http://gnss1.tudelft.nl/dpga/`

[7] `https://gssc.esa.int/navipedia/index.php/Time_References_in_GNSS`

[8] GPS (Global Positioning System) Time - `https://confluence.qps.nl/qinsy/9.0/en/utc-to-gps-time-correction-32245263.html`

On the other hand, meteorological data is aligned with the atomic time UTC, an improvement of the UT1 time which is based on the diurnal motion of the Sun as observed on Earth. UTC is more uniform than solar time and better for keeping civilian time.
Since a solar day is slightly longer than 24 hours due to the slowing down of the Earth's rotation (86400 SI seconds) the insertion of a correction, *leap second*, is needed. In fact, today mean solar day is actually about 86400.0027 SI seconds long ((Teunissen et al., 2017), p. 29). This effect adds up to about 1 second to UT1 yearly. In such case, the leap second correction ensures that the difference between the UTC and UT1 readings will never exceed 0.9 seconds, letting UTC not drift apart.
Since the GPST beginning 18 leap seconds have been added to UTC to keep it close to UT1 and compensate for the slowing of the Earth's rotation. In such case GPST is now 18 seconds ahead from UTC. This correction needs to be taken into account when searching for possible correlation between GNSS and meteorological data sets by subtracting 18 seconds from the GPST or by cutting the considered UTC time period with 18 seconds shorter than the GPST period of interest.

4.2 Instruments configuration & Experimental setup

In this research project four low-cost dual frequency GNSS systems were installed on top of the EWI building in order to first prove their potential of high-accuracy positioning and test their capabilities for retaining wind-induced displacements of the case study building. As it can be seen in Figure 4 each module consisted of:

- u-blox ZED F9P receiver + u-blox antenna (1)
- Raspberry Pi Zero data logger (2)
- 2 x Micro USB cables (3a and 3b)
- OTG cable (4)
- 1 x 16 Gb SD Card (5)
- 1 x Waterproof plastic box (not shown in Figure 4)

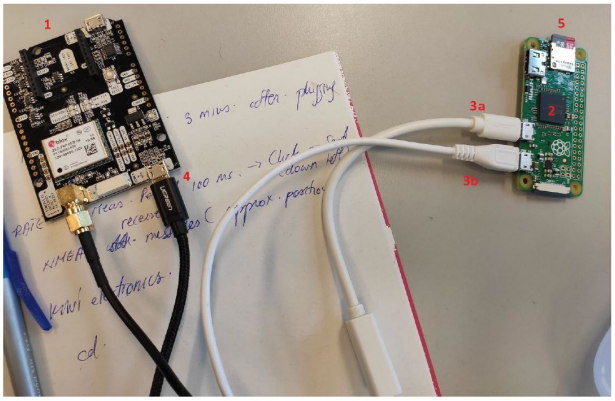

Figure 4. Low-cost dual frequency GNSS module components, u-blox receiver on the left and Raspberry Pi Zero data logger on the right

and was costing in total about 300 EUR.

Coming up to the description of the choice of the installation emplacement, the administrator of the radar equipment installed on top of EWI, Fred van der Zwan, offered two places for installing the GNSS modules. Both places were offering connection to 220V power supply and were in compliance with the safety protocol of the building.

Figure 5. GNSS modules placement on top of EWI building. Left side - installation on the South side of the roof top. Right side - installation on the middle part of the roof top. Both pictures are pointing to the South.

Since both locations were surrounded by tall measurement equipment, which partly obstructed the line of sight with the satellites, two modules were installed in a first location on the South side of the building roof top in between two radar antennas (EWI03 and EWI04, see left side of Figure 5) and the other two in a second location in a more centered position of the roof top surrounded by a control room and a tall radar antenna (EWI01 and EWI02, see right side of Figure 5). In this way the GNSS monitoring array could cover as much as possible from the building roof top area to see which location offers the best results for structural health monitoring purposes.

Figure 6. Emplacement of each antenna (surface type and GP or no GP). Metal disc as ground plane (GP). Each picture is pointing to the South.

Each receiver pair was installed in a waterproof plastic box together with the Raspberry Pi data loggers and three out of four antennas were screwed up on heavy concrete tiles which were supposed to follow any wind-induced moves of the building structure and behave with it as a whole body. The last one was mounted on a steel structure fixed to the building structure. It was thought that the steel structure could behave like a big ground plane and mitigate part of the multipath effect produced by the surrounding obstacles including the roof surface. This assumption will be further on discussed in the next chapter (see last part of subsection 5.1).
Also for mitigating this effect as much as possible metallic ground planes (GPs) were attached between two of the antennas and their concrete tiles. In addition, all antennas were all oriented in such a way that the "u-blox" logo was pointing in the South direction (see Figure 6).

An important note, that one needs to take into account for making the u-blox ZED F9P module acquire 10 Hz GNSS data sets, is on how to carefully configure the receiver via "u-center" software. Before any measuring campaign one should conduct data acquisition tests in order to see if the equipment acquires data at the wanted logging rate. In order to do so one needs to make sure that the GNSS receiver was correctly configured. For this two specific steps need to be conducted via "u-center", mainly to change the logging rate[9] and set-up large enough baudrate[10]. The later one makes the acquisition of data at higher logging rate (for e.g 5 Hz or 10 Hz) possible. In addition, after each configuration step one should send the configurations to the receiver via the "Send" button that can be found in the below left side of the Message View window of "u-center". Last but not least all configurations should be permanently saved[11].

5. DATA PROCESSING

5.1 GNSS Data Preparation & Processing

The four used GNSS modules were retrieving 24 hour .ubx observation files sampled at 10 Hz, which first needed to be converted to .rnx format[12], before starting with the data analysis. This has been done by using the convbin.exe CUI function of the RTKLib 2.4.3 package. Since the GNSS receivers were cutting the observation files after 24 hours but they all started at different time spans, one needed to generate 24 hour files spanning from 00:00:00 to 23:59:59 GPST for each day. This has been done by first splitting chunks from the .rnx files using convbin.exe, followed by splicing them together into 24 hour observation files (.obs) using another CUI executable called GFZRNX [13]. The final output .obs files were containing GNSS observations sampled at a 10 Hz rate over exact 24 hours for each day from 12/11/2019 until 02/12/2019.

For each day a 24 hour *triplet* of *one 10Hz .obs file*, *one 1-sec. DLF1 MO file* and *one DLF1 MN broadcast file* (for more details see subsection 4.1) was needed in order to perform PPK processing (see Figure 7).

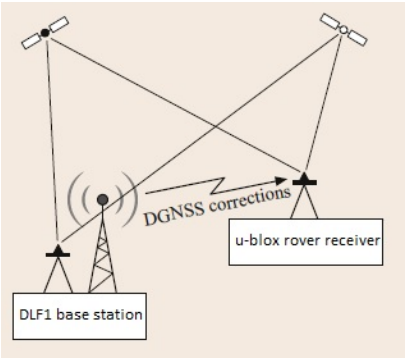

Figure 7. Differential GNSS (DGNSS) scheme for PPK processing, based on base station–rover correction transfer principle. Courtesy of ((Teunissen et al., 2017), p. 760)

The data sets were processed in rtkpos.exe software, part of the RTKLib 2.4.3 package. In the next line the chosen PPK processing configurations were listed. From the standard setup offered by rtkpos.exe one needs to perform following changes in the "Options" menu for pursuing PPK processing of dual frequency GNSS data:

- Setting1 - Positioning Mode: Single → **KINEMATIC**

  This setup specifies the GNSS processing method as PPK differential positioning (see chapter 2 and Figure 7 for more detail on this processing technique).

- Setting1 - Satellite constellation: **GPS**

  One decided to only rely on the GPS satellite constellation after identifying its sidereal day repeatability property (see last part of chapter 2) that can be used to determine the MP signature of each GNSS receiver and use it to mitigating part of this vicious effect.
  Note that, if one would like to use GPS together with Galielo constellation one would need to take into account that Galileo has a repeat cycle of 10 days and a revolution period of about 14 hours and 7 minutes[14]. In such a case the proposed procedure for identifying the MP signature of each receiver would not work when processing daily GPS and Galileo observations together. Though, this should work for every 10 days.

- Setting1 - Frequencies/ Filter Type: **L1+L2 Forawrd**

  This setup takes into account on GNSS observations from both carrier wave GPS bands, L1 and L2. In addition it specifies the Kalman filter type used for data processing. The forward filter type can be used in real time solutions. In this mode, the data is processed through the Kalman filter in forward direction from its beginning until the end just as the data was collected[15].

[9] step-by-step procedure: View/ Message View/ UBX/ CFG/ RATE/ Measurement Period.

[10] step-by-step procedure: View/ Message View/ UBX/ CFG/ PRT/ select UART1/ select 921'600 Baudrate.

[11] step-by-step procedure: View/ Message View/ UBX/ CFG/ CFG/ select 0 – BBR, 1 – FLASH, 2 – I2C – EEPROM, 4 – SPI-FLASH/ click on Send button.

[12] the Receiver Independent Exchange (RINEX) 3 format is a data interchange format that supports raw GNSS data of all major GNSS constellations (s.a GPS, GLONASS, Galileo, BeiDou, QZSS, IRNSS/NavIC and SBAS).

[13] download of GFZRNX.exe and manual at: `http://semisys.gfz-potsdam.de/semisys/scripts/download/index.php`.

[14] `http://www.positim.com/galileo_overview.html`

[15] `https://rtklibexplorer.wordpress.com/2017/08/21/ppk-vs-rtk-a-look-at-rtklib-for-post-processing-solutions/`

- Setting1 - Elevation Mask: **15°**

  This setup cuts down all GNSS signals coming from an elevation angle below 15 degrees. This was needed since most of the low elevation signals have a low signal-to-noise ratio and are more suspectible to multipath, hence they mostly corrupt the output positions.

- Setting2 - Integer Ambiguity Res (GPS/ GLO): **CONTINUOUS**

  As being mentioned before, carrier phase observations were preferred in this study simply because they can offer millimeter accurate position estimates in comparison to metre accurate solutions offered by pseudorange (code) observations. "The carrier wave for the GNSS signal is a sine wave with a period of less than one metre"[16] which repeats on its way from the transmitting satellite to the GNSS antenna. Measuring the phase of the carrier wave can reach millimeter precision, but the measurement is ambiguous since the total number of cycles between satellite and receiver is unknown. This process is known as **carrier phase ambiguity**. Resolving/ estimating the carrier phase ambiguity is the key to achieve accurate positioning. This paragraph further presents the choice of the most suited method for fixing carrier wave ambiguities for this case study.
  The choice of the ambiguity fixing algorithm can influence the final results and dependents on the type of GNSS application. In this case from the three offered methods of the RTKLib 2.4.3 package (Continuous, Fix and Hold and Instantaneous) the Continuous method was preferred. In order to understand what is the difference of all three methods, they were briefly presented in the next lines.
  Fix and Hold algorithm works on the principle of "feeding information derived from the current observation epoch forward to subsequent epochs one step farther"[17].
  Therefore, if for some reason RTKLib wrongly fixes one ambiguity, subsequent epochs could be also wrongly fixed. This procedure works the best with very accurate and trustful GNSS data where one would like to find a fixed solution and constrain it for a longer time until ambiguity resolution gets lost. Since low-cost GNSS equipment was used in this project this ambiguity solving method is not optimal.
  The **Continuous** algorithm feeds each previous float solution in a Kalman filter to continuously update the estimated phase biases on the basis of the current epoch's measurements and fix the ambiguities second by second. In such case every previous float solution is computed and feed into a Kalman filter as current states to repeatedly fix the ambiguity. This procedure is working well with low-cost equipment.
  On the other hand, the **Instantaneous** algorithm tries to fix the ambiguity every second without using any previous information. The latter method for sure will not have a large fixed ambiguity rate on GNSS data sets acquired by low-cost GNSS modules.
  In order to make a wise choice on the most optimal ambiguity fixing method a first set of observations spanning over 13/11/2019 (day of year (doy) 317) and 14/11/2019 (doy 318) were processed using PPK by testing each ambiguity fixing method. The daily mean values were subtracted from the resulting position time series and plotted against Greenwich Mean Stellar Time (GMST) time in order to capture the 24 hour stellar/ sidereal day repeatable MP effect which is "leaking" in the relative positions and residuals. For keeping the document structure clear only the East relative position time series of EWI03 GNSS module were presented in Figure 8. The ambiguity fixing rate (Q1) of each method was equal to:

  - **Fix and Hold**: day 317 Q1 = 91%, day 318 Q1 = 90%
  - **Continuous**: day 317 Q1 = 86%, day 318 Q1 = 84%
  - **Instantaneous**: day 317 Q1 = 47%, day 318 Q1 = 78%

  After a visual and statistical comparison of the results from Figure 8 one decided to use the Continuous method for ambiguity fixing since it offered the smallest estimated East root mean square error and the smallest number of vertical lines from each plot. As it was expected the Fix and Hold method yielded more miss fixed solution in the form of vertical lines while the Instantaneous method could solve a limited amount of ambiguities (gaps correspond to float ambiguities) increasing the position estimate uncertainties.

- Output - Solution Format: Lat/Lon/Height → **E/N/U-BASELINE** (ETRF2000 DLF1-EWI0X baseline vectors output format)

  This setting outputs the estimated relative positions as ETRF2000 baseline vector values between DLF1 base station and each EWI0X GNSS receiver.

- Output - Output Solution Status/ Debug Trace: Off → **Residuals**

  This setting makes the ouput of resiudal values possible.

- Positions - Base station: **X/Y/Z – ECEF (m)**

  The coordinates of DLF1 base station need to be manually input in rtkpos.exe. For any land surveying and geodetic activities it is recommended to change them with the ETRF2000 solutions which can be found at: `http://gnss1.tudelft.nl/dpga/coordinates.html`.

- Misc - Time Interpolation of Base Station Data: **TICK**

[16] = 19 centimetres for L1 band and 24.4 centimetres for L2 band; `https://www.novatel.com/an-introduction-to-gnss/chapter-5-resolving-errors/gnss-measurements/`

[17] Improving RTKLIB solution: Fix-and-Hold, `https://rtklibexplorer.wordpress.com/category/rtklib/fix-and-hold/`

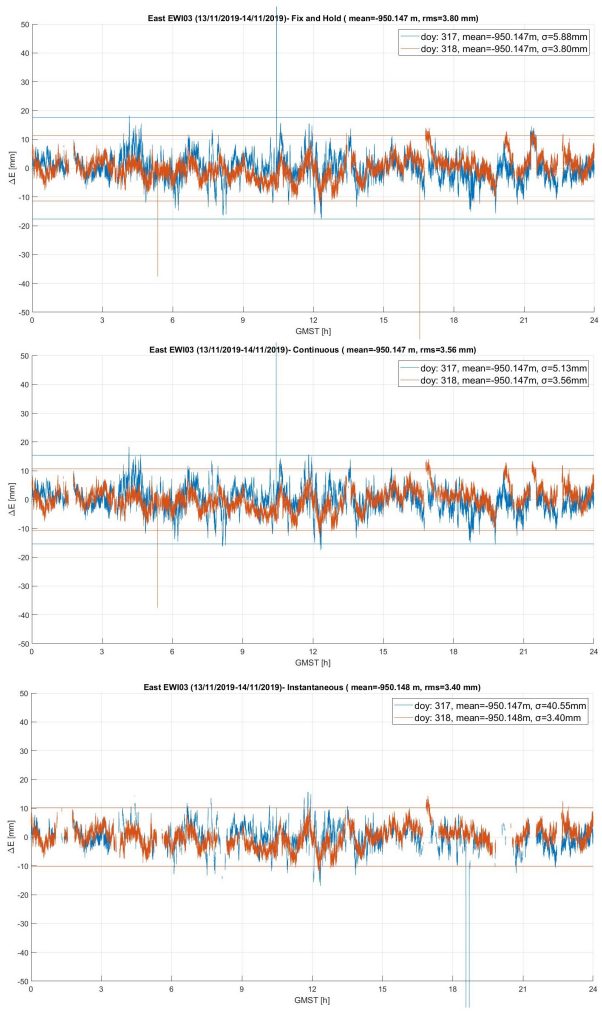

Figure 8. Comparison of the Fix and Hold (above), Continuous(middle) and Instantaneous (below) ambiguity fixing method. Overlap of EWI03's relative position estimates time series, with respect to their mean, of day 317 and 318.

This setup interpolates the 1-second observations of DLF1 MO file to 10 Hz sample rate and it is highly needed for 10 Hz processing.

The PPK processing configurations described above were saved in a .conf file and were summarized in the next Figure 9. These configurations were used for processing all acquired GNSS data sets.

RTKLib PPK processing configuration	
Positioning Mode	Kinematic
Sat. constellation	GPS
Frequencies/ Filter Type	L1+L2 Forward
Elevation Mask	15°
Integer Ambiguity Res	Continuous
Output - Solution Format	E/N/U- Baseline
Output - Output Solution Status/ Debug Trace	Residuals
Base Station: DLF1, Coords. ETRF2000 at epoch 2013-07-02 12:00	
X (ECEF) [m]	3924698.116
Y (ECEF) [m]	301124.8036
Z (ECEF) [m]	5001904.995
Misc - Time Interpolation of Base Station Data	Tick

Figure 9. Final PPK processing configurations.

After the first attempts on processing 10 Hz GNSS data sets one decided to down sample the daily .obs files from 10 Hz to 1 Hz. For this rtkpos.exe has an "Interval" option for down sampling the obs. file during processing. This has been done after finding out that rtkpos.exe could not process daily 10 Hz GNSS files returning instead an "insufficient memory" error message. After running several processing tests it was concluded that when using a personal computer with a processor of 8 Gb RAM and 2.4 GHz speed one can only process 2 hours of 10 Hz data, 9 hours of 5 Hz and 12 hours of 1 Hz data. When doubling the amount of RAM of the processor of the computer the amount of data that can be processed increases, giving the possibility to process 4 hours of 10 Hz data, 12 hours of 5 Hz data and 24 hours of 1Hz data. Under these circumstances, although one was interested in processing daily 10 Hz data sets in order to spot possible wind-induced deflections and vibrations of the EWI building, 24 hours files of 10 Hz observations were down sampled to 1 Hz. It is important to understand the limitations of RAM capacity of personal computers to keep the research project costs as low as possible.

Another, more expensive, alternative for performing full day 10 and 5 Hz data processing are super computers. Luckily Delft University of Technology possesses such advanced technology in the form of a HPC cluster of Linux computer servers with a lot of processing power developed by the Intelligent Systems Department (INSY) department[18]. Hence by establishing a Secure Shell (SSH) connection with the HPC cluster via a graphic client such as PuTTY[19] and installing the RTKLib 2.4.3 package on the server run[20], one could choose for a general partition for launching data analysis jobs, with a short Quality of Service (QoS)[21], of daily 10 Hz files or down sampled 5 Hz or 1 Hz files. The run time for a job took approximately 40, 20 respectively 11 minutes and the output solutions were returned in .pos files with a sampling rate of 10, 5 respectively 1 Hz. Most of the acquired data sets were processed by using the HPC cluster at 10, 5 and 1 Hz sampling rate but because lack of time only the daily 1Hz outputs were used for the wind-induced deformation analysis from chapter 6.

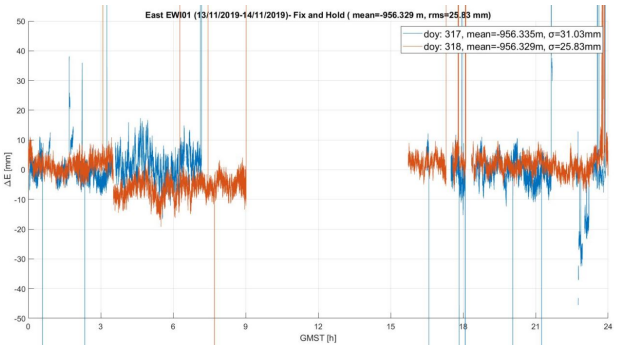

Figure 10. PPK processing test on EWI01 data set over doy 317 and 318. Data set is corrupt by showing large East root mean square errors, jumps and gaps in the time series

[18] https://login.hpc.tudelft.nl/

[19] for more information about the followed procedure see: http://insy.ewi.tudelft.nl/content/ssh-clients

[20] see RTKLib manual p. 88: http://www.rtklib.com/prog/manual_2.4.2.pdf

[21] for more information on the facilities that this QoS is offering see Partition and Quality of Service section from the HPC Power Point presentation:https://docs.google.com/presentation/d/10A0_0eNRBYd87E1h1YN6bsIFaZaua5qJkfBbnBKAr6o/present?slide=id.p

A final important comment on the validity of the data sets collected by EWI01 GNSS module should be made. After running several PPK processing tests it was identified that the EWI01 GNSS module data sets were corrupted since over one full day half of the ambiguities could not be resolved, which was translated in a big gap in the time series and a large East root mean square error. In addition, a lot of miss fixed ambiguity solutions could be identified as vertical lines in Figure 10, diverging from 0. It was believed that this happened because of the metallic structure on which EWI01 was installed. In such case it did not mitigate the MP effect as one expected, but it created more trouble corrupting the acquired GNSS signals. Hence, one cannot trust the data sets acquired by EWI01 and they should be excluded from this study.

5.2 Meteorological data processing

The meteorological data set provided by R. van Puffelen over 12/11/2019 – 02/12/2019 needed to be processed in order to extract valuable information about days with no/ low wind and rain activity and about days with intense wind activity. This information was used in order to pick three days with the lowest recorded wind speeds and no rain activity. Under such stable meteorological conditions one was expecting no deflection of the EWI building and nominal MP effect "leakage" in the relative position and residual estimates.
The following information presented in Figure 11 was used in order to draw a final conclusion on the days with low wind speed and little precipitation.

Low WS					Less precipitation	
Day No	doy	Min 1h avg. WS (m/s)	24h avg. WS (m/s)	max WS (m/s)	Precipit per day (mm/24h)	Max rainfall rate (mm/h)
30	334	0.2	0.8	3.9	2.03	2.00
20	324	0.3	1.4	7.8	NaN	NaN
16	320	0.4	1.1	6.0	NaN	NaN
17	321	0.7	2.1	6.2	NaN	NaN

Figure 11. Days with low wind speed and little precipitation (ordered in ascending order of 24 hour averaged wind speed values).

The first part of the table from Figure 11 contains the maximum wind speed (WS) record and two averaged values of WS, the first one related to the minimum from the 1 hour averaged WS values and the second one to a daily averaged WS value, over different days. The WS values were averaged over 1 respectively 24 hours since these time intervals were suggestive to point out which days were wind-still.
In the second half of the same table, information related to the amount of precipitation per day and maximal rainfall rate per hour were presented. In order to compute the precipitation values and determine the volume of water within each drop an assumption on the shape of the raindrop was made. Hence, one took into consideration that the raindrops had a spherical shape. By using the formula of the volume of a sphere and the drop size (DS)/ diameter measurements (expressed in millimetres) one could compute the corresponding volume of water in each drop. These values were averaged out over each hour and expressed in qubic metres per hour.
In order to convert the volumetric quantities in rain rates expressed in millimetre per hour, one divided the volumetric values by the catchment area of the disdometer of 0.0015 $[m^2]$ and multiplied by 10^3. (see equation 13).

$$rain\,rate = \frac{(\sum_{each\,hour} \frac{4}{3} * \pi * (\frac{DS}{2} * 10^{-3})^3)}{0.0015} * 10^3 [\frac{mm}{h}] \tag{13}$$

By taking the resulting rainfall rate values into account, in the next step one could compute the amount of precipitation per day expressed in $[\frac{mm}{24h}]$ by summing all rainfall rate values over 24 hours.
Summarizing the information from Figure 11 one decided to use day 320 (16/11/2019), 321 (17/11/2019) and 324 (20/11/2019) (highlighted in turquoise) in order to determine the 24h sidereal MP signature of the horizontal relative position time series for each receiver, which will be further subtracted from the horizontal relative position time series of the other windy days to correct for the MP effect and remain with the influence of the wind on the case study building.
Days 320 and 321 were two consecutive days over which no precipitation was recorded. By this no amplification of the MP effect was expected during these days (note that wet environments increase the effect of MP since they have a bigger scattering power). Furthermore, day 324 was chosen as the third day of interest instead of 334, since it was not containing any trace of precipitation as well. Though it is important to mention that day 323, previous to 324, was identified as the 5th most rainy day from the entire period of study. This could have an influence on the GNSS antennas installed in the middle part of the roof top (EWI01 and EWI02) after observing that this part of the building roof was retaining rainwater for a longer time than the other place where EWI03 and EWI04 were installed. In order to avoid any MP amplification induced by puddles filled with rainwater around the GNSS antennas a decision on fully relying only on data sets belonging to EWI03 GNSS module was taken. EWI04 GNSS module data sets were kept as a backup since this module was installed without a ground plane (see Figure 6), closer to one of the radar antennas being prone to larger MP.

High WS					More precipitation	
Day No	doy	max WS (5min avg,) (m/s)	avg WS (24h avg,) (m/s)	max WS (m/s)	Precipit per day (mm/24h)	Max rainfall rate (mm/h)
27	331	10.3	2.3	25.3	32.56	8.10
19	323	6.0	1.5	23.9	18.33	6.27
29	333	6.3	2.5	23.8	8.27	6.41
26	330	4.2	2.7	14.8	3.10	2.46
14	318	4.9	1.9	12.9	0.00008	0.00008

Figure 12. Days with high wind speeds and significant precipitation (ordered in descending order of 24 hour averaged wind speed values).

In accordance with the procedure for finding wind-still and zero-precipitation days, two windy days needed to be picked as well. The information from Figure 12 was used in order to draw a final conclusion on the days with high wind speeds. This time one used a smaller WS average window of 5 minutes, which is more relevant for identifying days with high wind speed activity since high WS values were not encountered very frequently. From Figure 12, days 323 (19/11/2019) and 331 (27/11/2019) (highlighted in turquoise) were picked for this study. Over these days maximal WS measurements of 23.9 and 25.3 $\frac{m}{s}$ were recorded which correspond to 6 Beaufort strong

breezes[22].

In addition to this a collection of suggestive plots for the windy days 323 and 331 were developed in order to obtain the most out of the meteorological data set:

- **Plots of the raw DS measurements against UTC time**

  These plots were used for identifying the exact times when rain fell during day 323 and 331. In addition, a similar plot was created for day 334 (30/11/2019).

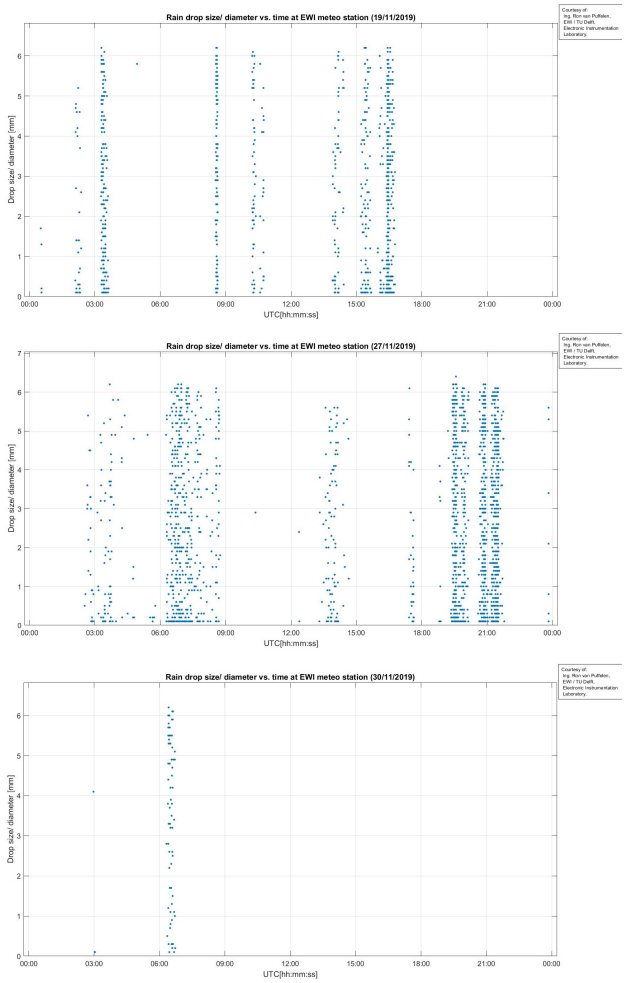

Figure 13. Raindrop size vs. UTC time over day 323 (top), 331 (middle) and 334 (below)

From Figure 13 one could immediately label day 331 as a more rainy day than 323. Day 334 was the only day with less wind activity and little precipitation (around 06:19 UTC) that was taken into consideration in the preliminary selection of wind-still days (see Figure 11).
The start and stop times can be useful to inspect if any horizontal relative position time series was deviating from a zero-precipitation time series during or after rain. In such case one can conclude that the MP effect was amplified by the wet environment around the antenna of receiver EWI03. Such visual analysis was taken into consideration in the next chapter between day 320 and day 334 (both wind-still days) .

- **Plot of the the 5 minutes averaged WS records of the wind-still and windy days**

  This plot illustrates the difference in WS magnitude between windy days 323, 331 and wind-still days 320, 321, 324.

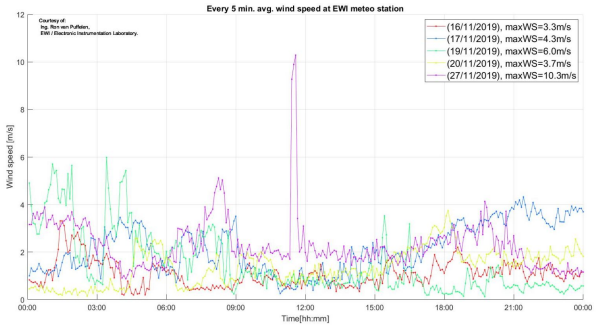

Figure 14. 5 minutes average WS vs UTC time plot of windy days 19 (323-green) 27 (331–magenta) and wind-still days 16 (320–red), 17 (321-blue)and 20 (324-yellow)

- **Plots of the $\frac{mm}{h}$ rainfall rate vs UTC time**

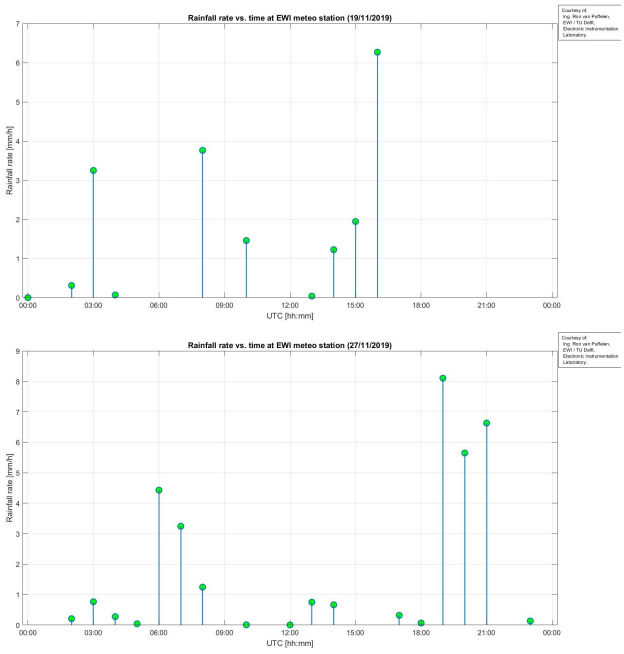

Figure 15. $\frac{mm}{h}$ rainfall rate vs UTC time plots of days 323 (top) and 331 (below)

These plots show the hourly amount of precipitation for each windy day. They further prove that day 331 was a more rainy day than 323, and at the same time they show when the rain activity peaked. For day 323 more rain fell in the late afternoon while for day 331 the strongest rain activity was present in the evening.

[22] `http://home.kpn.nl/djansma1939/wissel_map/weten/windkracht.htm`)

- **Plots of every second WS values vs. UTC time**

  These plots are very important when searching for a statistical cross correlation between WS measurements and MP corrected relative position estimates (see subsection 6.2 and 6.3) in order to identify any position deviations of the building inferred by wind.

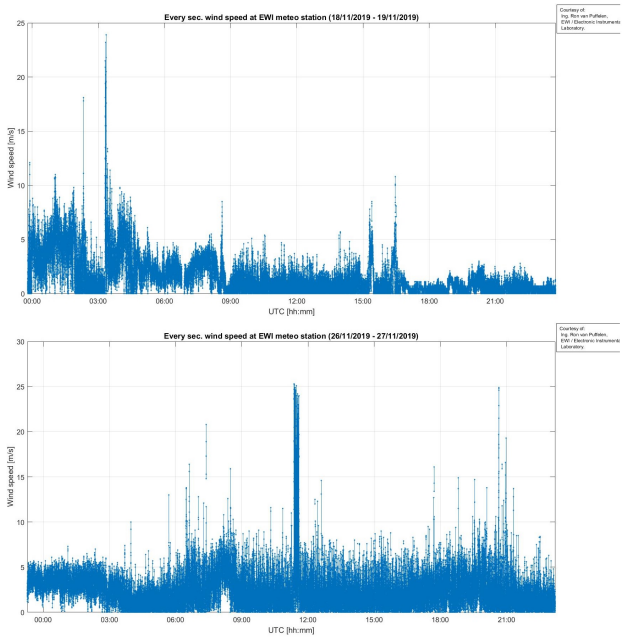

Figure 16. Every second WS measurements over day 323 (top) and 331 (below) against UTC

5.3 Multipath analysis

Multipath (MP) is one of the major error sources that influences the GNSS carrier phase (CP) measurements. It induces an erroneous effect which is "leaking" in the relative position and residuals obtained based on double difference observation estimation. This introductory discussion is meant to characterize the impact of MP on the accuracy of CP relative positioning to see if this vicious effect can infer an erroneous effect that exceeds centimetre order of magnitude making the identification of wind-induced displacements of the EWI building impossible.
In general, most of the GNSS error sources can be mitigated through differential PPK positioning between close-by rover- and base stations. But in case of MP this cannot happen since MP has a distinct influence on different GNSS antennas. Each GNSS antenna acquires signals coming from satellites that travel along different paths throughout the atmosphere. Depending on the surrounding environment most of the signals get also reflected and diffracted and are received later than direct signals. The signal reflection can get amplified by wet surfaces that have a bigger scattering power, hence the MP effect increases. To illustrate this a plot of the overlapping North relative position time series[23] of days 320 and 334 was created (see Figure 17). On its right side a short deviation (encircled in green) in the North relative position time series of day 334, with respect to the zero-precipitation North position time series of day 320, can be spotted. Looking over the last plot from Figure 13 one can concluded that this deviation was happening around 06:19 UTC, during rain.
Therefore, the travel time measurements[24], from which the GNSS receiver is able to determine positions[25], are disturbed by later received signals resulting in inaccurate position estimates.

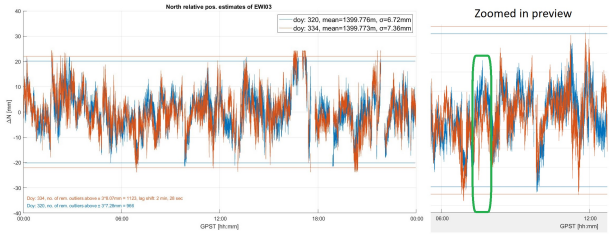

Figure 17. Overlap of North position time series of days 320 (zero-precipitation) and 334 (little precipitation around 06:19 UTC) vs GPST after applying lag shift (left side). Zoomed in preview in order to spot deviations (marked with green) between time series, around 06:19 UTC (right side)

This is how MP affects the position estimation procedure and makes it more complicated.
In general MP produces two effects:

- It influences the pseudorange (code) measurements used for estimating the ambiguity of CP measurements making this process last longer.
- Carrier phase MP is limiting the accuracy of baseline estimation.

In practice, its influence can be determined by applying some trigonometric formulas. This will be presented in the following lines.
In a MP environment, besides of the direct path signals, signals can be reflected and diffracted by obstacles of different shape. In most of the cases the relative delay (δ) of the signal can be determined by applying optics rules and trigonometry. In this paper only the general case of signals reflected by the ground was discussed. In this case when one is considering that the GNSS signal was reflected by the ground surface, δ can be computed as a function of the height of the antenna (h) and of the elevation angle (θ) of the satellite (see Figure 18)

$$\delta = 2 * h * sin(\theta)\ [m] \tag{14}$$

Since the antenna of the EWI03 GNSS module was installed on a concrete tile on the roof top of EWI building, one can consider h=5 cm. In such case the largest MP delay happened when the satellite was exactly overhead (see left side of Figure 19). Right after, the relative delay value was converted to MP relative phase (θ_m) by dividing it by the wavelength of L1 GPS signals[26] and multiplying it by 2π. This angular quantity was used in order to compute the phase error (θ_c) of the composite received signal (direct + reflected) which is tracked by the carrier-tracking loop of the receiver. To be mentioned that the direct signal has no influence on θ_c.

[23] the time series corresponding to day 334 was shifted to the right in order to align with the time series of day 320. This procedure was further described in subsection 5.3.

[24] = pseudorange(code) and carrier phase observations.
[25] = baseline estimation.
[26] λ_{L1}=0.1905 m.

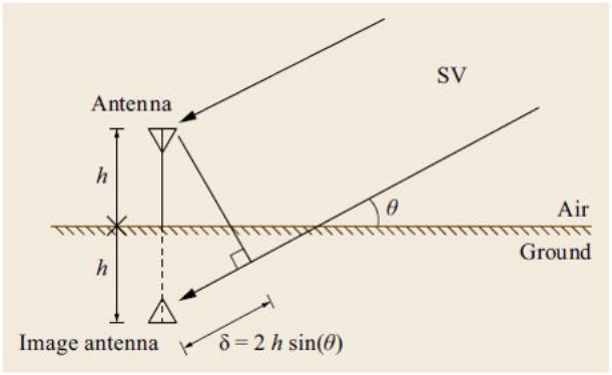

Figure 18. Relative delay as a function of h and θ (ground reflection case). Courtesy to ((Teunissen et al., 2017), p. 445)

For this the MP vector was decomposed into its orthogonal components (M_t, M_Q) as one can see in Figure 20. When omitting the influence of pseudorange MP, one can compute the resulting phase error θ_c by applying a simple trigonometric formula:

$$\theta_c = arctg(\frac{M_Q}{D + M_i}) = arctg(\frac{\alpha_1 * sin(\theta_m)}{1 + \alpha_1 * cos(\theta_m)}) \; [rad] \tag{15}$$

where $\alpha_1 = \frac{a1}{a0}$ is the relative amplitude of the MP which is computed as a ratio between the amplitude (a1) of the MP (= reflection coefficient of 0.5 corresponding to wet concrete) and the amplitude (a0) of the direct signal (= to 1). The values of the reflection coefficients correspond to values computed for a normal incidence angle ($\theta = 90°$, see (Teunissen et al., 2017) p. 445) but in this study they were assumed to be the same for each incidence angle.

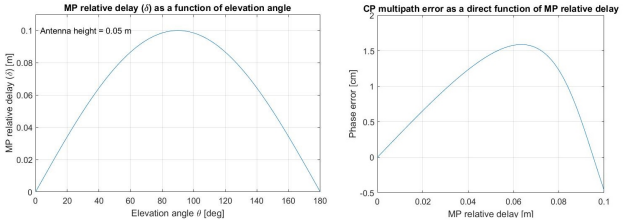

Figure 19. MP relative delay as a function of antenna height (h) and satellite elevation angle (θ), for h=5 cm (left). CP multipath error as a function of MP relative delay δ (right)

In the final step θ_c was converted back to metric units by dividing by 2π and multiplying with λ_{L1}. The resulting value corresponds to the CP error induced by MP of a ground reflected L1 signal. The CP multipath error was plotted as function of δ (see right side of Figure 19) reaching its maximum of $\approx$ 1.5 cm for δ=0.065 m when the satellite was at θ = 45 and 135°. Hence this erroneous effect can influence the accuracy of the position estimates with 1.5 centimetres. Of course in reality the composite received signal is much more complicated since the GNSS signal can be composed out of a multitude of signals reflected by different surrounding obstacles, which can amplify the MP effect depending on their fabrication material. But this generic value can give a first idea on how much influence MP can have on CP positioning.

As a conclusion, "leakage" of MP effect in position time series can cause errors of centimetre order especially when one

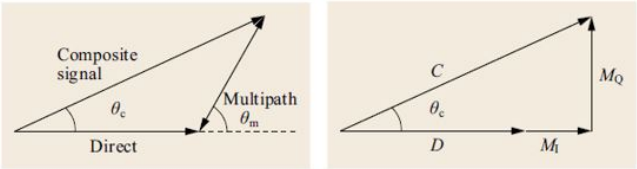

Figure 20. Figure of the phase (θ_c) of the composite received signal (left) and the decomposition of the MP vector into orthogonal components (right). Courtesy to ((Teunissen et al., 2017), p. 449)

is using low-cost equipment which is not built to the same standards as geodetic equipment for mitigating MP effect. If no action is taken, the expected hypothetical deflection value of 1.3 centimetres discussed in chapter 3 would be covered by MP noise making it impossible for any affordable dual frequency GNSS module to identify it. Therefore, a mitigation strategy is strictly necessary for high-accuracy positioning applications such as wind-induced deformation monitoring of tall buildings.

A final note was made on the behavior of the MP effect on CP measurements. When one wants to identify the MP pattern within a position time series, it might be beneficial to consider a longer time period (for example a full sidereal day) over which the MP effect will describe a rather slow behavior under the form of repetitive sinusoidal cycles making it more easy to be identified. Its repeating behavior makes MP act more like a deterministic time varying bias than a random bias. For larger δ resulting from slightly larger values for h (such as 50 centimetres), the phase error will follow this sinusoidal behavior which is characteristic for the MP effect (see Figure 21).

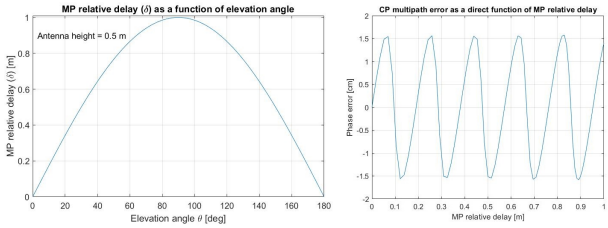

Figure 21. MP relative delay as a function of satellite elevation angle (θ), for h=50 cm (left). CP multipath error as a function of MP relative delay δ (right)

After having this extensive discussion about the effect of MP on CP PPK positioning, one can fully understand how MP effect behaves.

In the next step the MP signature withing the position time series of EWI03 GNSS module needed to be identified in order to correct for MP on position time series of windy days and identify possible wind-induced deflections of EWI building. This was done by using a property of the GPS constellation related to its sidereal day repeatability. This reads that if the satellite constellation repeats each sidereal day the MP effect of each satellite will repeat every day at the same time. In such case one could create plots of overlapping relative position time series of wind-still days and average their position solutions second by second in order to define the MP pattern. The only condition that needs to be satisfied is to make sure that the satellite configuration is kept identical over the wind-still days. If so, the patterns described by the relative position time

series should overlap (van der Marel, 2017). In reality the overlapping graphs will not entirely describe the same pattern since the MP effect reacts differently based on meteorological conditions on site. For example, this effect will be highly amplified if the surrounding area of the GNSS module is wet (see right side of Figure 17).
Hence, one needs to overlap the 1 Hz relative position time series of the identified wind-still days, 320, 321 and 324 and average them in order to define the MP pattern of EWI03 GNSS module. This pattern should be used on the windy days to separate the deformations and vibrations of the case study building, tracked by the GNSS equipment, by simply subtracting it from the relative position time series of the windy days, 323 and 331.

Throughout this process a first correction needed to be applied on the daily 1Hz RTKLib .pos output files. This correction was related to the fact that EWI03 GNSS module did not store exactly 86400 measurements per day. This was caused by possible **receiver cycle slips** driven by a discontinuity in the receiver's continuous phase lock, which could have been caused by:

- Receiver outage (for example power loss or unintentional restart making the fixed integer ambiguity resolution get lost)
- SD-card logger issue of Raspberry Pi (in this case the ambiguities were resolved and would not get lost during the period when the logger was not saving data)
- RTKLib processing problems on the position solutions (caused by unknown reasons that make the position solutions not converge)
- Dynamic obstructions (animals or people blocking the line of sight of the antenna over long periods, letting the GNSS signals not being tracked. In the end this would cause a loss of the fixed integer ambiguity)

In such case one needed to identify the missing time instants during each day of interest and fill the time and horizontal position coordinate gaps with NaN values. For this a Matlab script was implemented which searches for gaps in the time series of each day and updates the entire RTKLib .pos structure with NaN values corresponding to the missing time instants.
In the next step, **created-sidereal wind-still days** with matching relative position time series needed to be generated. But for this one first needed to decide which time frame should be used along with the GNSS data sets for identifying the MP signature. Beforehand, in Figure 8 the daily relative position estimates were plotted against GMST in order to capture the 24 hour stellar/ sidereal day repeatable MP effect which was "leaking" in the relative positions and residuals. As being presented in the previous discussion about MP behaviour, the GPS constellation repeats its geometry each mean sidereal day[27] if same satellite geometry is kept.
One mean sidereal day is the time it takes for the Earth to complete one rotation about its axis with respect to a "fixed" star, while one mean solar day[28] "is the time interval between two consecutive passes of the Sun across the observer's meridian" ((Teunissen et al., 2017), p. 28). The later one is approximately 4 minutes longer because of the extra needed rotation of the Earth caused by the orbital revolution about the Sun in order to get the Sun aligned with the observer's meridian. Hence UTC runs approximately 4 $\frac{minutes}{day}$ slower than GMST time. This means that when one is using civilian UTC time frame, the GPS satellites will reach same position on the sky 4 minutes *earlier* each day. This time shift will exist also when comparing UTC based meteorological data sets with GNSS data sets aligned on the GMST time frame. In such a case if one is not correcting for the 4 $\frac{minutes}{day}$ shift with passing time, the daily GMST origin will diverge more and more from the 00:00:00 UTC origin making it much more complicated for the readers to identify any correlation between the GNSS and UTC based meteorological data sets. For example 00:00:00 of UT1/UTC time on the 16th of November 2019 (day 320) corresponded to 03:39:07.6874 GMST and 00:00:00 UT1/UTC of the following day (day 321) corresponded to 03:43:04.2427 GMST (see Figure 22). In such a case by plotting the relative position estimates against GMST, as in Figure 8, one was not automatically correcting for the 4 $\frac{minutes}{day}$ shift to align the time in such way that the GPS satellites would rise and set at the same moment every day. Hence, this would have made the inspection for finding any correlation between the UTC based meteorological data and the GMST based GNSS data more complicated.

Figure 22. Conversion of UT1 to GMST, GAST and ERA for day 320(left) and 321(right) (`https://dc.zah.uni-heidelberg.de/apfs/times/q/form`)

Therefore, from now on all plots based on GNSS data sets were aligned on the GPST time frame. Note that for correcting on the time shift of 18 leap seconds between UTC and GPST, the meteorological data sets were shifted with 18 seconds back in time (for more information inspect last paragraph of subsection 4.1).
Taking into account on the information presented above one could start to generate overlapping created-sidereal days from the relative position time series of days 320, 321 and 324. In order to perfectly match the horizontal relative position time series of the wind-still days 320, 321 and 324 and define the MP signature of EWI03 GNSS module one needed to select an origin day and cut it in such a way that it covers a full sidereal day (00:00:00 - 23:56:04.0905). Since day 320 (16/11/2019) was the first wind-still day from the days of interest, it was chosen to be the origin day. For the next day (321) one needed to take into account that the next sidereal day would start at 23:56:04.0905 UTC of previous day (320) and would end at approximately 23:52:08 UTC of the current day. This means that for each wind-still day one needed to add and subtract **3.931825 minutes * number of elapsed days from the origin day** from the start and end time instant of day 320. This has been done in order to *capture the same geometry of the GPS satellites with respect to the origin day* and was labeled as created-sidereal day cut procedure. Figure 23 shows exactly this shift applied to days 321 and 324 with respect to day 320

[27] one mean sidereal day corresponds to 23h 56m 04:0905s in solar time (UTC).
[28] one mean solar day corresponds to 24h 03m 56:5554s in sidereal time.

taking only into account on the time instants corresponding to ambiguity fixed position estimates. This is the reason why several gaps can be observed along each daily time series.

Figure 23. Time shift of each wind-still and rain less day wrt. day 320. This plot takes only into account on the time instants of ambiguity fixed position estimates

After generating these created-sidereal days over which the horizontal position time series patterns should have perfectly aligned, a check on the satellite geometry integrity over the freshly created-sidereal days was needed. In order to check this, one checked the similarity between the plots showing the number of satellites over the wind-still days. Figure 24 proves that during these three wind-still days the GPS constellation geometry configuration was kept almost the same at any time.

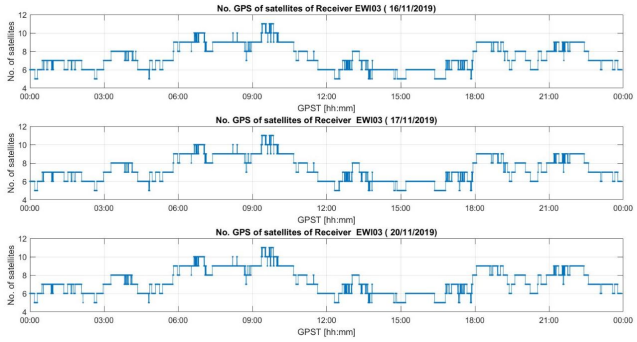

Figure 24. Number of satellites vs. GPST during day 320 (top), 321(middle), 324 (below))

In the last step before plotting the daily relative position estimates of days 320, 321 and 324 on top each other, two filtration steps were applied. The first one eliminated the estimated relative positions that:

- had their horizontal coordinate formal standard deviation σ_{dE}, σ_{dN}[29] values above 1.5/ 1.5 centimetres.
- had a lower number of tracked satellites than 5.
- were based on float ambiguities.

[29] computed based on the least-square functional model by rtkpost.exe.

The second filtration step[30] was used to remove the relative positions related to miss fixed ambiguity solutions (e.g illustrated as vertical lines spread away from 0 in Figure 8) which exceeded the $3\hat{\sigma}$ criterion:

$$|dE/N - \overline{dE/N}| > 3 * \hat{\sigma}_{dE/N} \quad [31] \tag{16}$$

Last but not least, the daily mean was removed from the remaining relative position estimates in order to center the time series around 0.

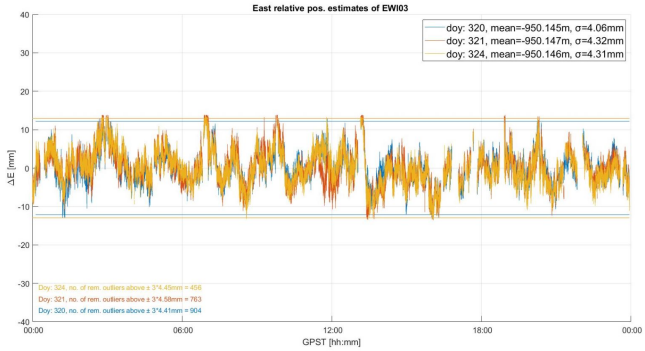

Figure 25. Overlap of East position coordinate time series of days 320, 321, 324 vs GPST of the origin day 320 without applying any lag shift. Contains no. of removed estimates after second filtration (see lower left corner).

When looking over Figure 25 one could see how good the patterns of the horizontal relative position estimates of days 321 and 324 were aligning with respect to the origin day 320. But since this creation of sidereal days was a pure mathematical process, where one was appending and cutting a certain amount of minutes from neighboring days, there might exist some physical processes, such as the gravity field of the Earth, the luni-solar gravitational attraction, atmospheric drag, solar radiation pressure ((Teunissen et al., 2017), p. 1292) and thruster events for reposition the satellites on their original orbit, that can perturb satellites[32] from following their nominal orbital motion and introduce lags between daily horizontal relative position time series. To check if there was any lag between the horizontal position time series of days 321 and 324 with respect to 320, the normalized cross correlation as a function of lag time was computed using Matlab's **xcorr** function (see Figure 26). This function was able to identify a lag of 11 seconds between day 320 and 321 and a lag of 35 seconds between day 320 and 324. To support this, Figure 26 was proving a very strong normalized cross correlation, between both pairs of days, indicated by the sharp and narrow peaks and by the close-to-one maximum cross correlation values from the legends. It is worth noting that for a positive lag value the time series of the second input day should be shifted to the right in order to perfectly match with the relative position time series of the origin day.

In addition, Figure 27 shows an example of the original East position coordinate time series and the lag shifted East position coordinate time series of day 324 with respect to 320. When

[30] note that this filtration step cannot be used in case of real-time processing since one first needs a 24h position time series in order to compute its mean and formal standard deviation value.

[31] the *empirical* standard deviation values were computed based on the horizontal position coordinates time series after applying first filtration.

[32] these perturbations can differ from satellite to satellite.

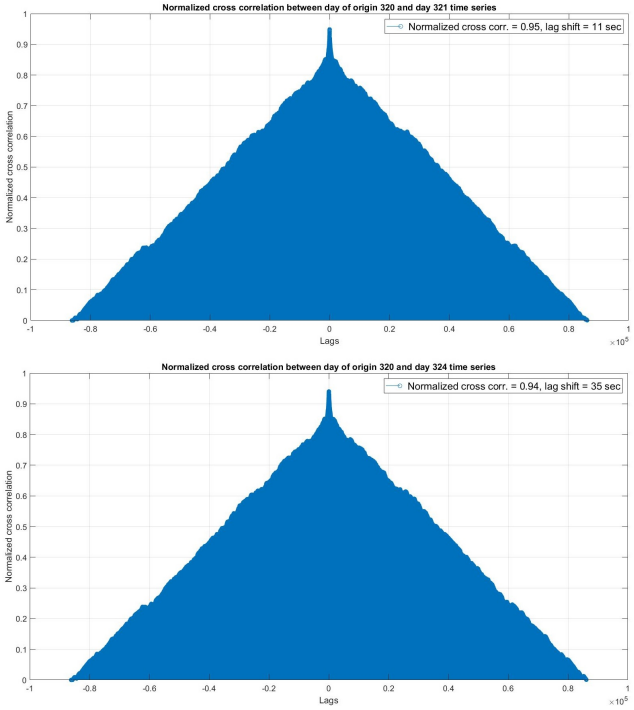

Figure 26. Normalized cross correlation plots of days 321 (top) and 324 (below) wrt. origin day 320. Maximal cross correlation value and lag shift are presented in legends

comparing the M-shaped pattern from the last part of the relative position time series from both images one can conclude that there was some physical influences on the orbital motion of the satellites which caused a slowdown of 35 seconds of the satellites during day 324 with respect to day 320.
In order to fully correct for this, one needed to take into account on each lag value when generating the created-sidereal days. But because of lack of time the procedure of implementing this final correction within the created-sidereal day creation procedure will be recommended to be developed in further studies. For now, the lag values of each day of interest with respect to the origin day were applied on the GPST time measurements without taking them into account when generating the created-sidereal days, leaving small lag-gaps at the beginning of the overlapping horizontal position coordinate time series.

Figure 27. Zoomed in preview of the original (top) and lag shifted (below) overlay of the East position estimates of days 320 and 324. Plot suggests that lag shift correction is necessary on day 324. See M-shaped pattern at the end of each time series

Following the above presented reasoning, the lag shift procedure was applied to the horizontal relative position estimates time series of the created-sidereal days 321 and 324 in order to determine a fully corrected time series of wind-still days. The resulting overlap can be seen in Figure 28. In this figure the values of the filtered out solutions exceeding the $3\hat{\sigma}$ criterion, together with the applied lag values were plotted as well in the lower left corner.

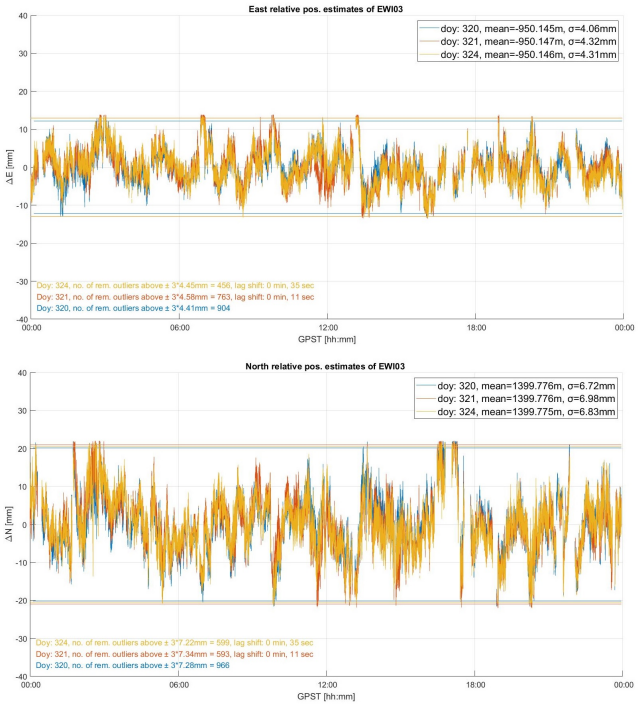

Figure 28. Day 320, 321, 324 overlap of horizontal relative position estimates time series (fully corrected for lag shifts and unwanted solutions) vs GPST of the origin day 320

Having three pairs of horizontal relative position estimates spanning over full sidereal days (86165 samples $\rightarrow$ 00:00:00 - 23:56:04.0905) one needed to average them second by second in order to define the final MP signature of EWI03 GNSS module. Since filtration- and cycle slip based gaps occur at different time instances during the days of interest, a NaN mean operation was used which is not taking into account on the NaN values. This procedure will not influence the final result since all three wind-still days should describe identical horizontal relative position time series.
The averaged out horizontal position time series were subtracted by their daily mean values in order to center them around 0. The resulting MP pattern of EWI03 on both East and North directions is visualized in Figure 29.

Note that according to the variance law by averaging the relative position estimates time series of days 320, 321 and 324 on each horizontal direction, the standard deviation of the MP signature time series should get smaller:

$$\sigma_{dE/N_{MP}} = \frac{1}{3}\sqrt{\hat{\sigma}^2_{dE/N_{320}} + \hat{\sigma}^2_{dE/N_{321}} + \hat{\sigma}^2_{dE/N_{324}}} \tag{17}$$

$$\sigma_{dE_{MP}} = 2.44\,mm,\ \sigma_{dN_{MP}} = 3.95\,mm$$

These values proved to be smaller than the actual empirical

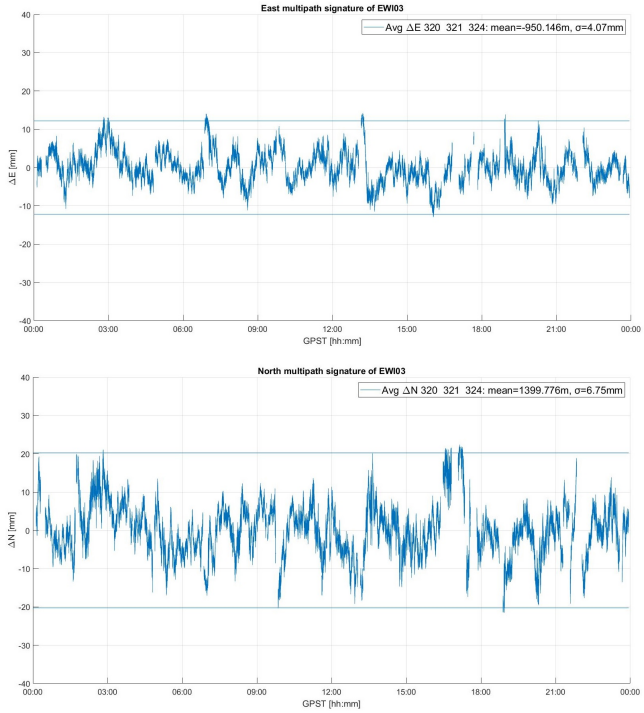

Figure 29. MP signature on East and North direction of EWI03 GNSS module

standard deviation values determined by Matlab's **std** function which can be found in the upper right corner of Figure 29. This happens to be so, because the variance propagation law takes into account that the East and North MP signature time series were influenced only by random noise while in reality these time series were still containing most of the MP effect. The systematic time varying effect of the remaining MP effect was found in the empirical root mean square error values from Figure 29. Hence they were larger than the propagated standard deviation values.

5.4 GNSS data sets of windy days. Determining the wind-induced deformation time series

As being presented in subsection 5.2, day 323 (19/11/2019) and 331 (27/11/2019) were picked as windy days for this study. As being said, over these days maximal WS measurements of 23.9 and 25.3 $\frac{m}{s}$ were recorded, corresponding to 6 Beaufort strong breezes.

Part of the correction procedure described in the last part of the previous subsection was applied on the horizontal relative position estimates time series of days 323 and 331 as well. The adopted principles from the previous correction procedure consisted of appending NaN values to the entire .pos structure corresponding to the indices related to the missed observation intervals followed by the first filtration procedure (see subsection 5.3) of the unwanted horizontal relative position estimates. The remaining horizontal relative position solutions were subtracted by their corresponding daily horizontal coordinate mean values in order to centre them around 0.

In addition, a second filtering procedure, different from the one presented in subsection 5.3, was applied. This time the procedure was not based on the $3\hat{\sigma}$ criterion anymore but on mitigating all **dE/N – mean(dE/N)** values exceeding 5 centimetres. Values that were exceeding this threshold describe unlikely motions of the building and were most likely produced by cycle slips and miss fixed ambiguities. Moreover, if the difference between consecutive horizontal coordinate values were larger than 3 centimetres the outlier values were filtered out as well.

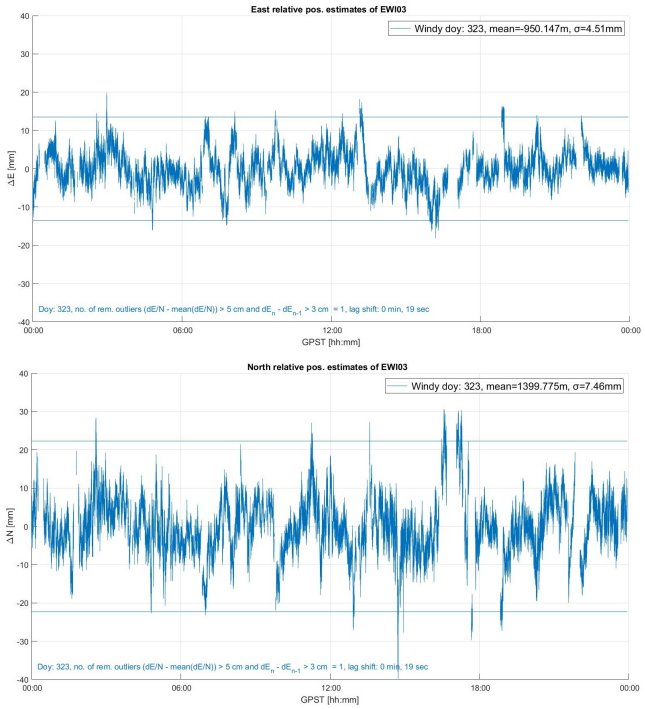

Figure 30. Relative position time series on East and North direction of windy day 323

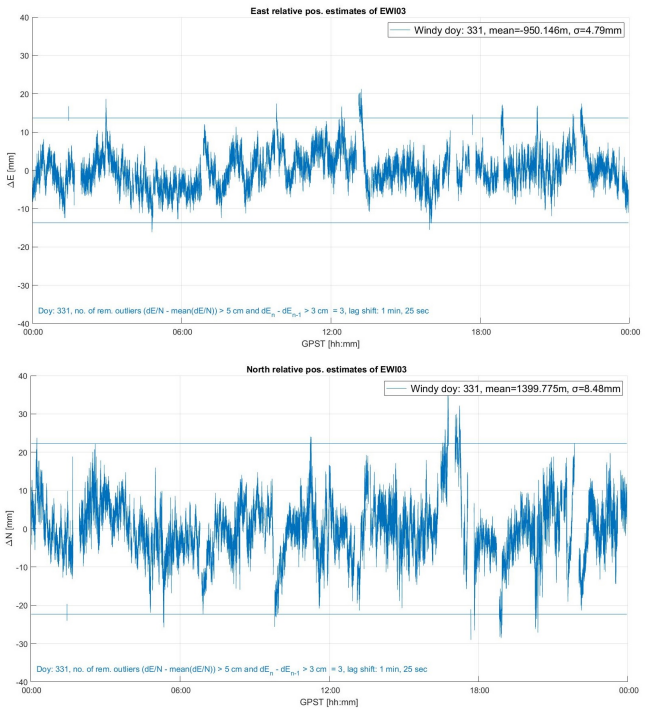

Figure 31. Relative position time series on East and North direction of windy day 331

Last but not least, the normalized cross correlation lag between the relative position time series of the windy days and the MP signature were applied in order to shift the horizontal relative position time series of day 323 and 331 to correspond with the MP signature time series (aligned with respect to the origin day 320). The **xcorr** function was able to identify a lag of 19 seconds between the MP signature- and day 323 horizontal relative position time series, and a lag of 85 seconds between the MP signature- and day 331 horizontal relative position time series. The number of removed outliers after the second filtering step and the lag shift were plotted as well and can be seen in the lower left corner of Figure 30 and 31. A quick look on the satellite geometry integrity of the MP pattern and the windy day position time series was studied as well using similar plots as the one from Figure 24. Also in this case the GPS constellation geometry configuration was almost the same at any time along the MP signature- and windy days time series.

After determining the MP pattern of EWI03 GNSS module (see subsection 5.3) and the 323 and 331 windy day relative position time series, one was interested to correct for the MP effect and remain only with the wind-induced deformation time series (dE/N_{WND}). In order to do so, the East and North MP pattern values (dE/N_{MP}) were subtracted from the windy days values (dE/N_{323} and dE/N_{331}) second by second[33]. But through this subtraction the noise level of the resulting wind-induced deformation time series increased.
According to the variance propagation law the standard deviation values of the wind-induced deformation time series over day 323 and 331 were equal to:

$$\sigma_{dE/N_{WND_{323/331}}} = \sqrt{\hat{\sigma}^2_{dE/N_{323/331}} + \hat{\sigma}^2_{dE/N_{MP}}}$$

$$\begin{aligned} \sigma_{dE_{WND_{323}}} &= 6.07\,mm,\ \sigma_{dN_{WND_{323}}} = 10.04\,mm \\ \sigma_{dE_{WND_{331}}} &= 6.11\,mm,\ \sigma_{dN_{WND_{331}}} = 10.04\,mm \end{aligned} \tag{18}$$

These values show that the noise level increased after subtraction. Though, the variance propagation treats the MP effect as a random error although the MP error behaves more like a deterministic time varying bias, which is acting slower over longer period with every repeating sinusoidal cycle (remember discussion about MP behavior, see Figure 21). Therefore, since the formula of the variance propagation law should normally take into account only on random errors the above calculated values might be unrealistic. When comparing them with the empirical standard deviation values (see (19)) computed by Matlab's **std** function over a full day, one can identify a consistent difference between them.

$$\begin{aligned} \hat{\sigma}_{dE_{WND_{323}}} &= 3.13\,mm,\ \hat{\sigma}_{dN_{WND_{323}}} = 4.63\,mm \\ \hat{\sigma}_{dE_{WND_{331}}} &= 4.17\,mm,\ \hat{\sigma}_{dN_{WND_{331}}} = 5.37\,mm \end{aligned} \tag{19}$$

The empirical standard deviation values (19) are computed based on the MP corrected horizontal position estimates of day 323 and 331, and prove that the MP correction was successful since these values are considerably smaller than the expected standard deviation values from (18).

[33] Figure 30 - Figure 29 for day 323 resulting in Figure 32 and Figure 31 - Figure 29 for day 331 resulting in Figure 33.

In addition, the plots of the wind-induced deformation time series prove the increase in noise since their random noise band got larger (see Figure 32 and 33) in comparison to all previous relative position plots (such as the one from Figure 30 and 31). These plots were plotted against the real recorded time of day 323 and 331, and not against the time corresponding to the origin day 320 as all previous relative position plots.

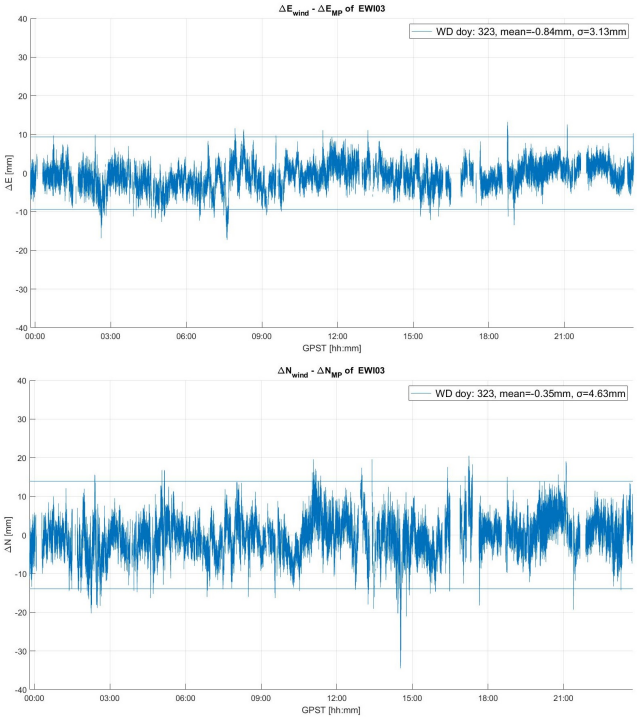

Figure 32. Wind-induced deformation position time series (corrected for MP) on East and North direction of windy day 323

5.5 Coordinate system transformations (conversions) and wind direction conventions

5.5.1 From ETRF2000 DLF1 coordinate system to across/along$_{EWI}$ (AccAl$_{EWI03}$) coordinate system

Since all GNSS data sets were processed in PPK mode with DLF1 base station as origin by using its ETRF2000 solutions at epoch 2013-07-02 12:00 (see Figure 9), all GNSS based relative position estimates from this study were positioned within ETRS89's solution, ETRF2000. Their corresponding coordinate system (CS) had as its origin DLF1's antenna with its axes pointing in North (Y-axis) and East (X-axis) directions (see Figure 34).
As a side note, the European Terrestrial Reference System 89 (ETRS89) is the European recommended reference frame for mapping and surveying applications that was defined to coincide with ITRS (International Terrestrial Reference System) at epoch 1980.0 and was fixed to the stable plate of the Eurasian Plate making it a regional Earth-Centered, Earth Fixed geodetic Cartesian reference frame.

For this study there is a better ETRF2000 based coordinate system to be used for identifying possible wind-induced horizontal deformations of EWI building. This coordinate system was defined as a local 2D-Cartesian coordinate system with its origin at the position occupied by EWI03's antenna and the X and Y axes defined along and across the EWI building.

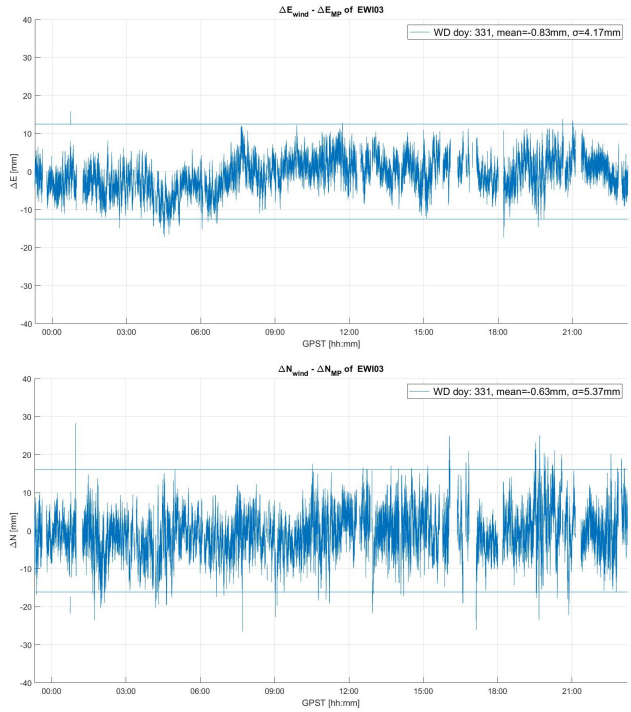

Figure 33. Wind-induced deformation position time series (corrected for MP) on East and North direction of windy day 331

From now on this local coordinate system was called AccAl_{EWI03}.
Hence, a conversion between ETRF2000's DLF1 and AccAl_{EWI03} CS was needed. The steps from bringing any ETRF2000 DLF1-EWI03 relative position estimates to AccAl_{EWI03} are:

- **Coordinate system origin translation. From DLF1 to EWI03 origin**

  The previous created wind-induced deformation time series plots (see Figures 32 and 33) resulted by subtracting the MP signature time series from the horizontal coordinates time series of windy day 323 and 331. By this, one was involuntary translating the resulting wind-induced deformation position estimates from their original coordinates system of the measurements centered at DLF1 base station to AccAl_{EWI} local system centered at EWI03 rover station.
  From a mathematical point of view the translation happens if one subtracts any relative coordinate time series by the mean of the horizontal position time series of the chosen wind-still days (320, 321, 324) with little rain[34].
  In such a case when this principle was applied on each term on the right side of (20), the mean(dE/N_{MP}) value acted like a constant which got simplified by the subtraction operation (see (21)):

$$dE/N_{WND_{323/331}} = dE/N_{323/331} - dE/N_{MP} \quad (20)$$

$$dE/N_{WND_{323/331}} = (dE/N_{323/331} - \cancel{mean(dE/N_{MP})}) - \\ - (dE/N_{MP} - \cancel{mean(dE/N_{MP})}) \quad (21)$$

- **Coordinate system rotation from East-North to across$_{EWI}$-along$_{EWI}$ directions**

  In order to identify and describe any wind-induced displacements of EWI building one was interested to rotate the daily wind-induced deformation time series ($\text{dE/N}_{WND_{323/331}}$) from East/ North directions to across/ along$_{EWI}$ directions.
  In addition to the GNSS estimates, the meteorological data sets of day 323 and 331 were treated as wind vectors with magnitude equal to the recorded WS and direction equal to the recorded WD. These vectors were then separated into U/ V – orthogonal wind components and rotated on the same across/ along$_{EWI}$ directions. The resulting values were labeled as $across_U$ and $along_V$.
  Last but not least, any possible statistical cross correlation between the two rotated pairs was subject of study in order to test the capabilities of the used dual frequency GNSS modules for measuring wind-induced displacements of the EWI building.
  In general, any 2D Cartesian coordinate system can be rotated by using a rotation matrix of the form:

$$R = \begin{pmatrix} cos\theta & sin\theta \\ -sin\theta & cos\theta \end{pmatrix} (CCW direction) \quad (22)$$

  This rotation matrix rotates any coordinate system in counter-clockwise (CCW) direction with θ degrees[35].
  In order to determine the azimuth angle of EWI building QGIS software was used for defining two points along the East façade of the EWI building (see Figure 34). For identifying the outline of the EWI building an open source topographic map from the Pdok (Publieke Dienstverlening Op de Kaart Loket) plugin[36] was used. Since this map was based on the Dutch coordinate reference system (CRS), EPSG:28992 - Amersfoort / RD New - Projected, one first needed to use QGIS coordinate transformation functionalities to transform the projected coordinates of the two points from RD to WGS84 CRS. Their WGS (World Geodetic System) 84 geographic coordinates were fed into (23) in order to compute the azimuth angle in need for rotating the wind-induced deformation position estimates and the U/V-orthogonal wind components.[37]

$$\theta = arctg\left(\frac{sin\Delta\lambda * cos\phi_2}{cos\phi_1 * sin\phi_2 - sin\phi_1 * cos\phi_2 * cos\Delta\lambda}\right) \quad (23)$$

[34] these daily mean values (mean(dE/N_{MP})) are describing a wind- and precipitation less state and were used for defining the MP pattern of EWI03 module.

[35] in this case θ represents the azimuth angle of EWI building.

[36] for more information about Pdok plugin visit: `https://github.com/rduivenvoorde/pdokservicesplugin`

[37] λ - geographic longitude, ϕ - geographic latitude.

$$where: \Delta\lambda = \lambda_2 - \lambda_1$$

In this case the azimuth angle θ was equal to 23.9504°. Knowing this value, each dE/N$_{WND}$ pair[38] of each daily time series was multiplied independently by the rotation matrix R in order to apply the CCW rotation (see (24)).

$$acc/alo_{WND_{323/331_i}} = \begin{pmatrix} cos\theta & sin\theta \\ -sin\theta & cos\theta \end{pmatrix} * \begin{pmatrix} dE_{WND_{323/331_i}} \\ dN_{WND_{323/331_i}} \end{pmatrix} \quad (24)$$

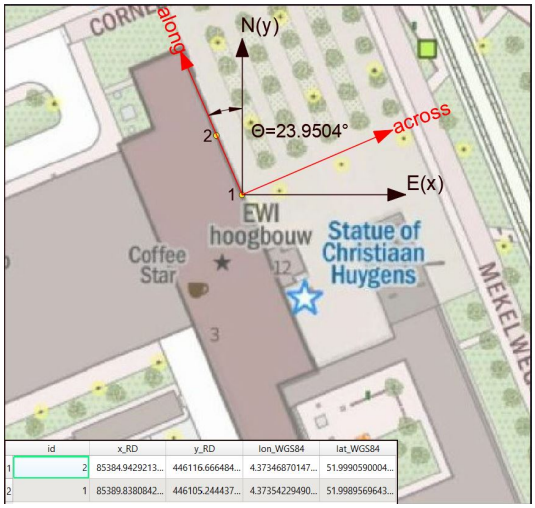

Figure 34. Rotation from North-East CS to across/along$_{EWI}$ CS based on θ

After rotating the wind-induced deformations time series of both windy days (across/along$_{WND}$), plots of them against GPST were created (see Figure 35 and 36).

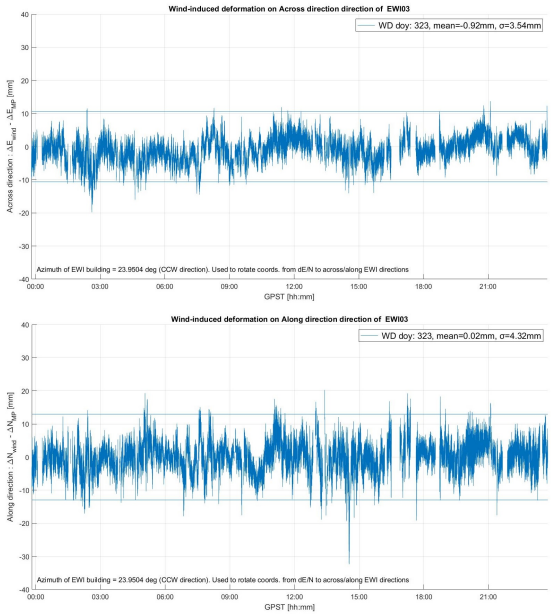

Figure 35. across/along$_{WND}$ time series of windy day 323 vs GPST

[38] each dE/N$_{WND}$ pair consisted of i=1$\cdots$86165 samples.

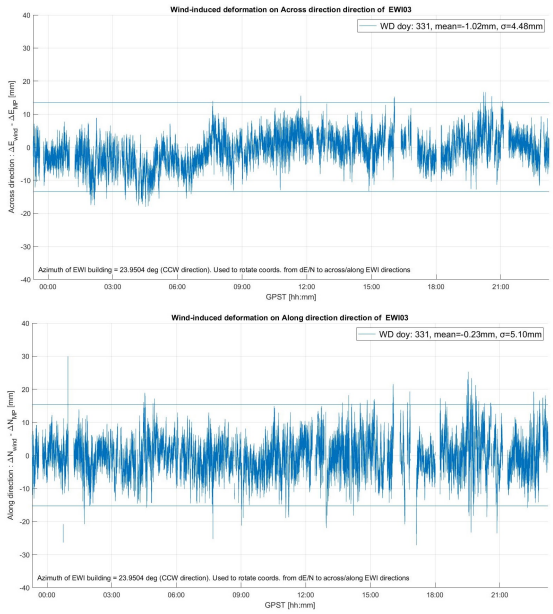

Figure 36. across/along$_{WND}$ time series of windy day 331 vs GPST

5.5.2 Separation of wind vector measurements into U and V orthogonal wind components

In the next step the wind vectors of day 323 and 331 were separated in U and V direction. For this, the meteorological wind direction values (mwd$_{WD}$, also know as wind barfs)[39] pointing from where the wind was blowing needed to be converted to math wind direction (md$_{WD}$)[40]by using (25). This operation was changing the clock wise orientation of the barf system to counter clockwise direction.

$$md_{WD} = 270° - mwd_{WD} \quad (25)$$

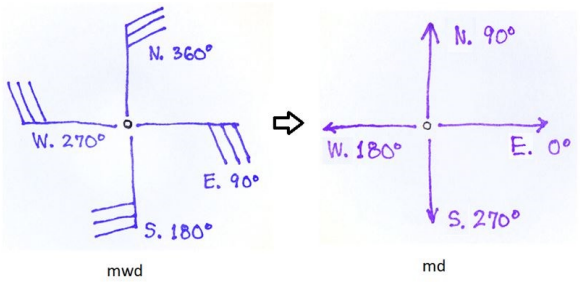

Figure 37. Conversion from mdw$_{WD}$ (wind barfs) to md$_{WD}$ (wind vectors). Courtesy of: `http://colaweb.gmu.edu/dev/clim301/lectures/wind/wind-uv`

If any resulting md$_{WD}$ value was less than 0 degrees, 360 degrees were added to avoid negative values. The resulting math wind direction values were suited for using them with mathematical equations and had a vector arrow convention pointing towards the direction the wind was

[39] point from where the wind is blowing: 0°-North, 90°-East, 180°-South, 270°-West, 360°-North.

[40] point towards which direction the wind is blowing: 0°-East, 90°-North, 180°-West, 270°-South, 360°-East.

blowing (see right side of Figure 37).

By using the WS and the md_{WD} values each wind vector from day 323 and 331 was split into U and V orthogonal wind component measurements using (26).

$$\begin{aligned} U &= WS * cos(md_{WD}) \\ V &= WS * sin(md_{WD}) \end{aligned} \tag{26}$$

Then by applying the same rotation matrix R on the daily U and V component time series as it is presented in (24), plots of the rotated $across_U$ and $along_V$ orthogonal wind components over day 323 and 331 against UTC time were created (see Figure 38 and 39).
An important comment on Figure 38 and 39 is related to the axes plotted on the right side of each figure. These axes show from which cardinal direction the wind was blowing. In such case, positive $across_U$ values correspond to wind measurements coming from West direction while negative values correspond to wind measurements coming from East direction. Following this principle, positive $along_V$ values correspond to wind measurements coming from South direction and negative ones correspond to wind measurements coming from North direction. This sign convention can be followed on the axes on the right side of each figure and is useful for identifying South-West and/ or North-East winds.
Note that this type of winds were of interest since they could produce displacements of the structure when hitting the building perpendicular on its glass walls. On the other hand, South-East and North-West winds face the concrete walls of EWI which are stiff and technically should not produce major displacements of the structure.

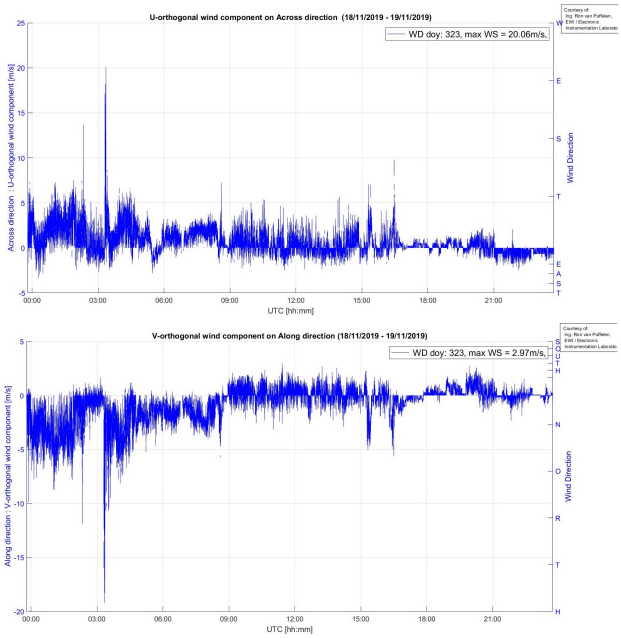

Figure 38. $across_U$ and $along_V$ orthogonal wind components of day 323 against UTC time. Right-side axes show from which cardinal direction the wind was blowing (wind barf convention)

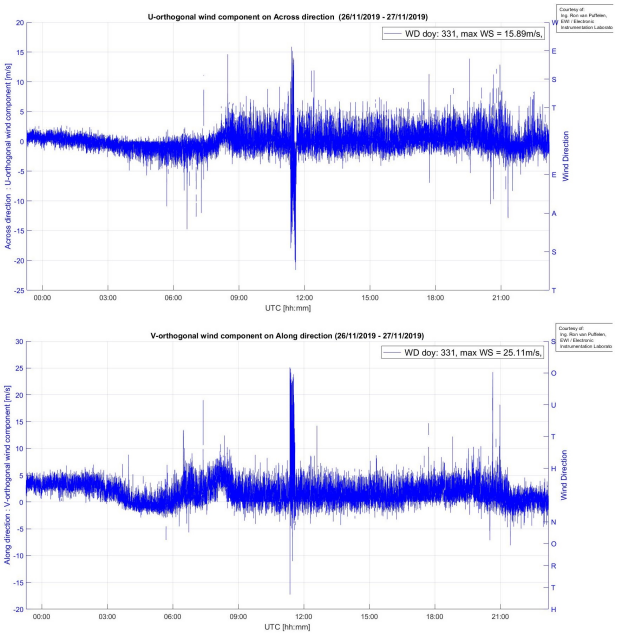

Figure 39. $across_U$ (top) and $along_V$ (below) orthogonal wind components of day 331 against UTC time. Right-side axes show from which cardinal direction the wind was blowing (wind barf convention)

6. WIND-INDUCED DISPLACEMENTS ANALYSIS

In the final step of this study one was trying answer both phrased research questions. Firstly, by analyzing some GNSS data sets of the EWI02 module being subject to artificial induced displacements in order to proof the capabilities of the newly released dual frequency GNSS module to sense permanent building displacements of centimetre order of magnitude.
Secondly, by aiming on a strong statistical cross correlation between the $across/along_{WND_{323/331}}$ horizontal wind-induced displacement time series and the $across_U$ and $along_V$ orthogonal wind component time series of both windy days 323 and 331.
Last but not least, by zooming in the time series of both types of data in order to pick specific time spans when the wind was blowing favorably from South-West and/ or North-East direction. In such cases, any correlation between GNSS based wind-induced deformation time series and wind measurements was anticipated.

6.1 Detection of artificially induced permanent displacements

It was known after the first PPK processing tests run on the GNSS data sets of all four dual frequency GNSS modules that one could rely only on the data sets coming from EWI03 GNSS module. As it was presented in the last part of subsection 5.1 and 5.2, the data sets of the other three remaining modules were omitted because of their installation emplacement. In addition to this explanations, it was known that EWI02's antenna was deliberately moved with 1.2 centimetres to the East in order to induce some artificial permanent deformation to see if the low-cost dual frequency GNSS module is capable of sensing it. By this, one could prove that low-cost dual frequency GNSS modules are able to sense permanent displacements of buildings in the order of centimetres.

While trying to determine the MP signature of this module by overlapping the relative position time series of wind-still days 320, 321, 324 with an extra wind-still day 334 (30/11/2019)[41], as being presented in subsection 5.3, it was found that EWI02's antenna was shifted with 1.6 $\pm$ 0.3 centimetres to the East and with 0.6 $\pm$ 0.5 cm to the North somewhere between day 324 and 334 (see legend of Figure 40).

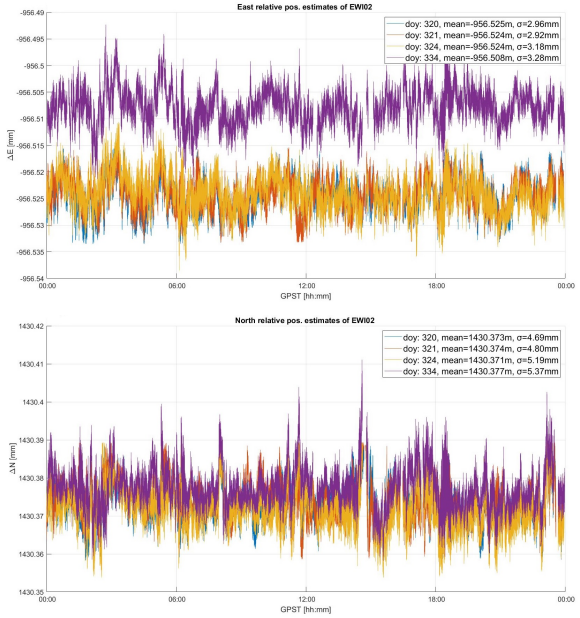

Figure 40. Horizontal relative position time series showing that EWI02 GNSS module was shifted 1.6 cm to the East (top) and 0.6 cm to the North (below)

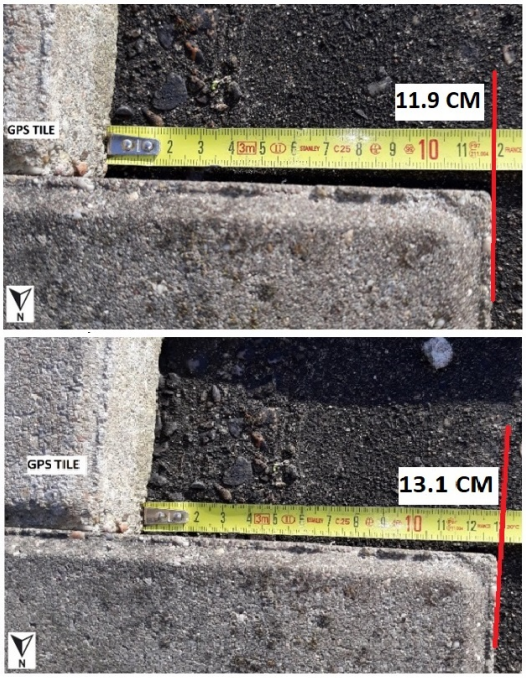

Figure 41. Ruler tape measurements of artificial induced deformation of 1.2 cm to the East (inferred on 25/11/2018)

[41] the choice of the wind-still days is motivated in subsection 5.2, see Figure 11 as well.

On 25/11/2018, while visiting EWI's roof top in order to save the data sets from the SD cards and clear them, this artificial deformation was introduced in a controlled manner. The introduced artificial deformation was measured twice with a ruler tape and by taking the mean of both measurements it was shown that in reality the concrete tile, on which EWI02's antenna was installed, was shifted with 1.2 centimetres to the East (see Figure 41).
The difference of 0.3 centimetres between the ruler tape measurements and the GNSS based mean relative position estimate in East direction could have been related to ruler tape measurement errors but also to the fact that the horizontal relative position time series from Figure 40 were not corrected for MP. The East root mean square error output of $\pm$ 0.3 centimetres shows that the estimated value of 1.6 centimetre lies within 1σ. Hence the estimated deformation value can be accepted.

This result proves that low-cost dual frequency GNSS modules are capable of retaining centimetre order permanent displacements of buildings without even correcting for MP effect. Although this outcome was artificially induced it proves that this type of GNSS equipment could be used for monitoring permanent displacements of tall buildings over long periods. In addition, previous results of this study show that when correcting for MP effect, one can make low-cost dual frequency GNSS equipment output sub-centimetre positioning accuracies even under 6 Beaufort winds stresses and under heavy rain of up to 8 $\frac{mm}{h}$ (see legends of Figure 32 and 33 and Y-axis values from Figure 16).

6.2 Statistical cross correlation between wind speed measurements and wind-induced displacements over full sidereal days

Since the possible perturbing factor of EWI's building position could have been South-West and/ or North-East winds, one was expecting from their random behaviour to not influence the position of the case study building permanently. Hence one was looking for short responses of the building to wind influences under the form of displacements and vibrations. Therefore, in the next step of the wind-displacement analysis a statistical normalized cross correlation between $across_{WND}$ and $across_U$ time series and between $along_{WND}$ and $along_V$ time series of both windy days was subject of study (correlation between Figure 35 and Figure 38 for day 323 and between Figure 36 and Figure 39 for day 331). In principle if for each windy day both time series pairs were strongly correlating this would attest that the perpendicular-to-EWI's glass façades wind vectors were causing significant deflections, traceable by the low-cost dual frequency GNSS modules.
For windy day 323 one was expecting from the highest correlation peak to have a lag equal with 19 seconds corresponding to the lag shift of windy day 323 with respect to the origin day 320. In case of day 331 the highest correlation peak was expected to be shifted to the right with 85 seconds corresponding to the lag shift of windy day 331 with respect to the origin day 320.
Figure 42 and 43 show contrary that between the rotated wind-induced deformation time series and the rotated orthogonal wind component time series of days 323 and 331 only poor statistical cross correlation values of 0.08-0.09 could be found. In addition, the lags of the highest correlation peaks were not close at all to the expected values. Therefore, it is hard to conclude that the EWI03 GNSS module was able to sense

wind-induced deflections of EWI building.

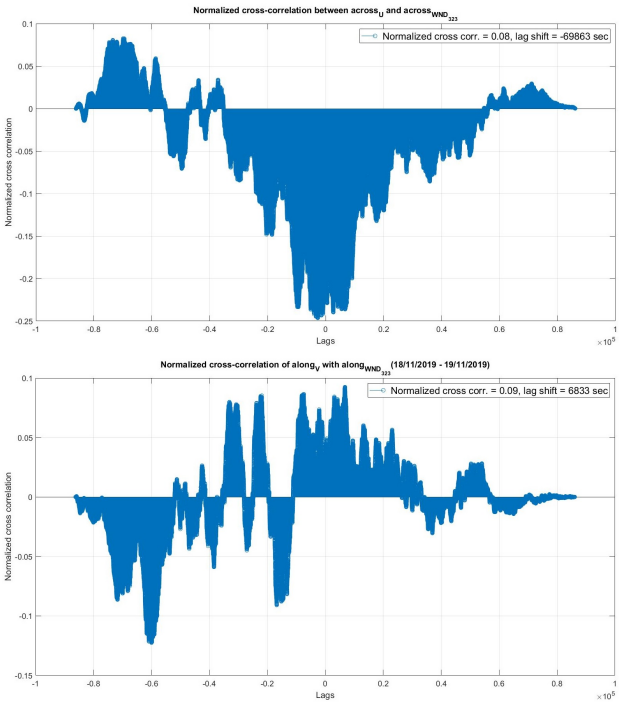

Figure 42. Normalized cross correlation vs. lags of *across*U and *across*$_{WND}$ (top) and of *along*V and *along*$_{WND}$ (below) of day 323

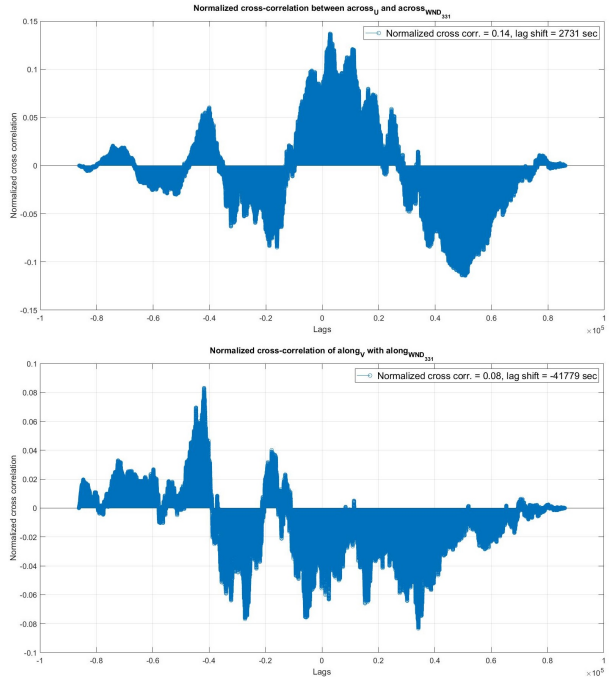

Figure 43. Normalized cross correlation vs. lags of acrossU and across$_{WND}$ (top) and of alongV and along$_{WND}$ (below) of day 331

The first explanation of these results can be related to the fact that meteorological factors such as wind directions have a rather random behaviour that will hardly follow any statistical rule.

Therefore, one searched for correlation between the rotated wind-induced deformation time series and the WS measurements of both windy days.

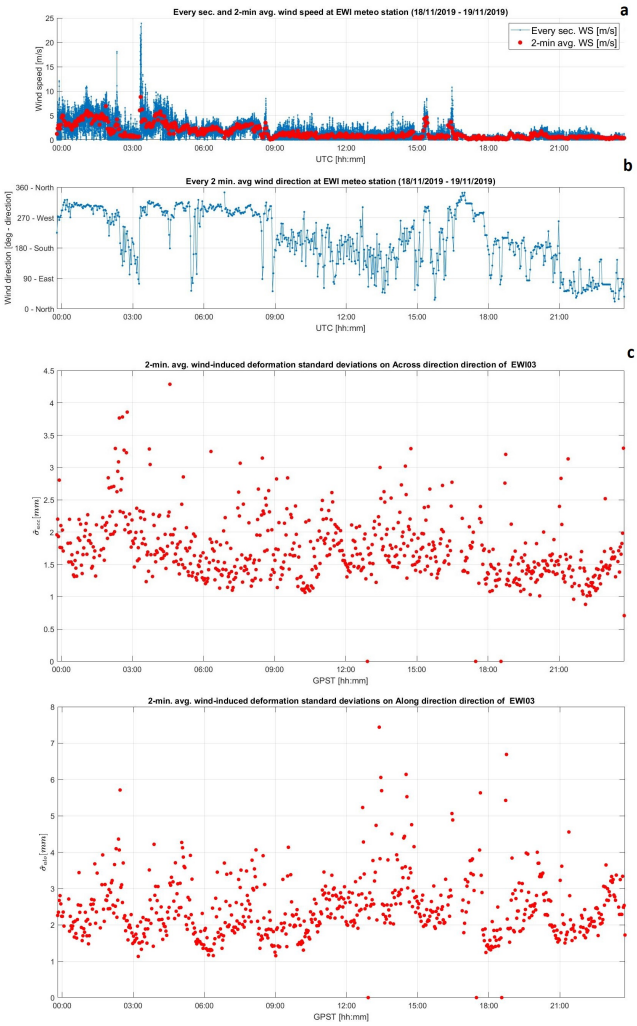

Figure 44. Temporal variation of 2 minutes mean values of WS and displacement responses of EWI building during day 323: a) 2 min. mean WS, b) 2 min. mean WD (most frequent value), c) 2 min. empirical standard deviation of the *across/ along*$_{WND_{323}}$ displacement time series

Firstly, for both windy days a plot collage inspired by (Tamura et al., 2002) was created. Each plot collage contained:

- **a) Every second and 2 minutes mean WS time series**
  This plot indicates when wind storms happened. Later the 2 minutes mean values were as well used for creating meaningful plots of the 2 minutes mean *across/ along*$_{WND_{323/331}}$ displacement variation with the 2 minutes mean WS variation (see Figure 46 and 47). At the end of this subsection this type of plots was used for identifying any correlation between the rotated wind-induced deformation time series (*across/along*$_{WND}$) and the WS measurements.

- **b) 2 minutes mean WD time series**
  This plot indicates more clearly the wind direction and its change during each windy day. But it might contain erroneous values. These values appear for averaged values

which are pointing over 2 minutes equally as much in the North-East direction as in the North-West direction. Therefore, it is recommended to confront it with the right side axes of Figure 38 (for day 323[42]) and Figure 39 (for day 331).

- **c) 2 minutes empirical standard deviation values ($\sigma_{acc/alo}$) computed based on the values within each 2 minutes window applied on the *across/ along*$_{WND_{323/331}}$ time series**
  This plot shows the *change in variance as a function of time* of the rotated wind-induced displacement signals, which is proportional to the square of the 2 minutes mean WS and WD values. Hence when the wind was blowing on average with significant WS values suffering a rapid change from any cardinal direction to South-West and/ or North-East, one expected from the standard deviation values to peak.

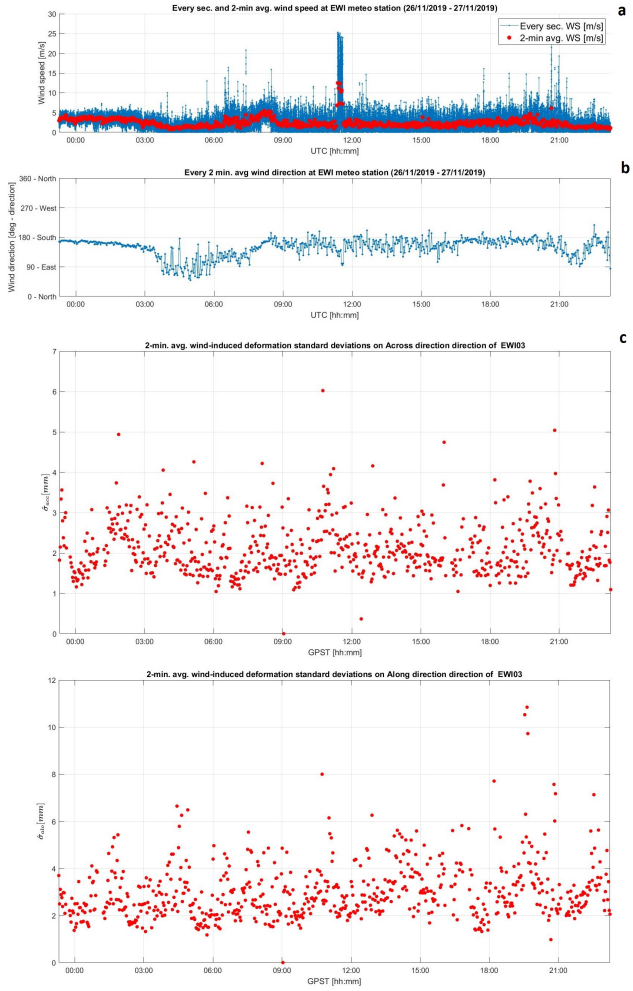

Figure 45. Temporal variation of 2 minutes mean values of WS and displacement responses of EWI building during day 331: a) 2 min. mean WS, b) 2 min. mean WD (most frequent value), c) 2 min. empirical standard deviation of *the across/ along*$_{WND_{331}}$ displacement time series

[42]this plot shows many WD changes during day 323, making this day very interesting for studying detection of displacements of EWI building.

In case of windy day 323 some correlation could be found between plot **b** and plots **c** from Figure 44. One could find that the highest σ_{acc} and σ_{alo} values peaked with rapid changes of wind direction from South-East to South-West around 03:00 UTC (see plot **c** of σ_{acc}) respectively from South-East to North-East around 13:30 UTC and from South-West to North-East around 18:30 UTC (see plot **c** of σ_{alo}).
On the other hand, the peaks from plots **c** did not correlate at all with the peaks of the WS measurements from plot **a**.

In case of windy day 331 less correlation could be found between plot **b** and plots **c** from Figure 45. In this case it was found that the highest σ_{acc} and σ_{alo} values peaked around the same times when the wind direction changed from South-East to South around 11:30 UTC and 20:30 UTC. Plot **b** shows that at that time the wind was blowing on average from South-East direction perpendicular to the concrete walls of the EWI building. Only during short periods of time the wind was blowing from South direction during which σ_{acc} and σ_{alo} values reached their maximum.
This time, the peaks from plots **c** showed some weak correlation with the maximum peak from plot **a** related to a 6 Beaufort wind breeze. This happened because of the permanently changing WD from South-East to South and back at that time (see plot **b** from Figure 45).

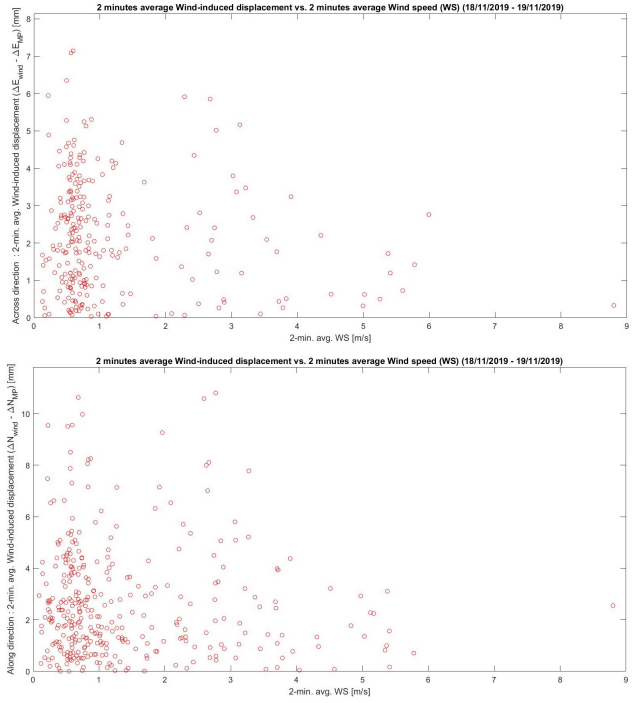

Figure 46. Variation of 2 min. *across/ along*$_{WND_{323}}$ displacement vs. 2 min. mean WS during day 323

Secondly, plots for each windy day consisting of 2 minutes mean *across/ along*$_{WND_{323/331}}$ - against 2 minutes mean WS time series were created (see Figure 46 for day 323 and Figure 47 for day 331). Their main purpose was to identify any correlation between the rotated wind-induced deformation time series and the WS measurements of both windy days. Hence if they show a linear growth of the displacement values with increase in WS, strong correlation between the data sets can be confirmed.

The 2 minutes mean *across/ along*$_{WND_{323/331}}$ values should capture any significant wind-induced displacements of the EWI building. These values were computed based on averaging *across/ along*$_{WND_{323/331}}$ values every 2 minutes.
In addition, they work as well as a moving average filter for removing part of the random noise from the across/ along wind-induced deformation time series, created by subtracting the MP signature from the relative position time series of each windy day (see last part of subsection 5.5).

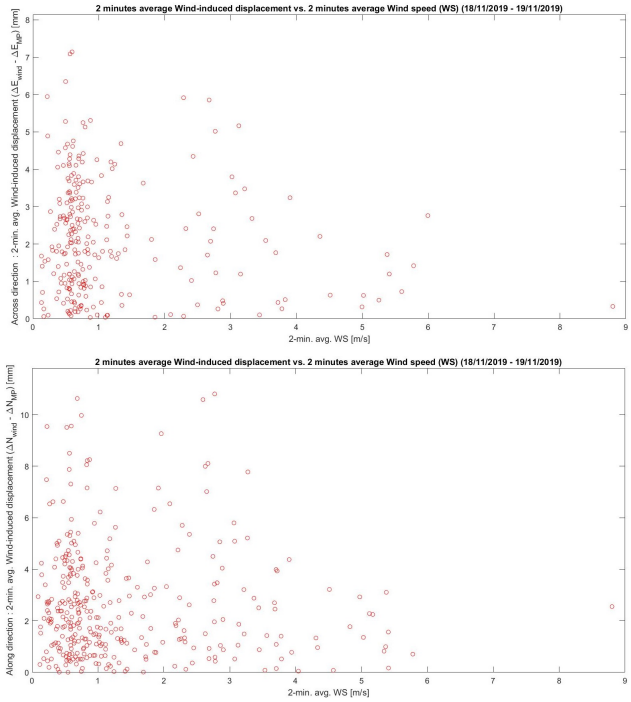

Figure 47. Variation of 2 min. *across/ along*$_{WND_{331}}$ displacement vs. 2 min. mean WS during day 331

Since both Figures, 46 and 47, show an exponential decay of scattered data points one could conclude that there is little to no correlation between the GNSS based wind-induced deflection data and the meteorological data of day 323 and 331. In conclusion EWI03 GNSS module could not identify notable quantities that can be related to wind-induced displacements of the case study building over day 323 and 331.

In the next subsection specific time periods, describing possible displacements, were selected based on wind measurements showing favorable wind directions (such as South-West and/ or North-East direction) and thorough inspected in order to find any correlation between GNSS based position estimates and wind measurements.

6.3 Exploratory analysis. In search for correlation over short time spans

In addition to the previous analysis steps a last attempt on identifying correlation between GNSS data containing possible wind-induced displacement patterns and wind data was made. In order to do so, specific time periods containing possible building displacements were chosen based on favorable wind directions and analyzed. For each windy day one example was discussed in the following lines.
In case of windy day 323 a 15 minutes time interval centred around 03:21:36 UTC was chosen. This specific time instant corresponded to the highest WS record (6 Beaufort breeze of 23.9 $\frac{m}{s}$) of day 323. At the same time the wind was blowing from West direction representing an ideal case for the displacement analysis. When carefully inspecting plot **b** from Figure 44 it was identified that during that period of time the wind was blowing on average from North-West direction, perpendicular to one of the concrete walls of EWI. This was verified by visually inspecting the right axes of both plots from Figure 49. The later figure was created based on spline interpolation of the *across*$_U$ and *along*$_V$ values over each second in order to fill the missing gaps of the meteorological data.
Nevertheless, on this specific time span a Matlab script was used in order to ask for the time instants of the South, South-West or West and/ or North, North-East or East winds that were hitting the glass walls of EWI perpendicularly. Over the chosen 15 minutes time interval only three time instants were found to be in accordance with these conditions. They were all corresponding to West winds with magnitude $\geq$ than 18 $\frac{m}{s}$[43] (see Figure 48).

S-SW-W direction meas.			
UTC	WD	WS	Cardinal dir.
3:20:15	272	20.2	W
3:21:26	278	19	W
3:21:36	279	23.9	W

N-NE-E direction meas.			
UTC	WD	WS	Cardinal dir.
None	None	None	None

Figure 48. S-SW-W (left) and N-NE-E (right) WD, WS measurements and cardinal directions inventory during 03:14:43 - 03:29:43, day 323

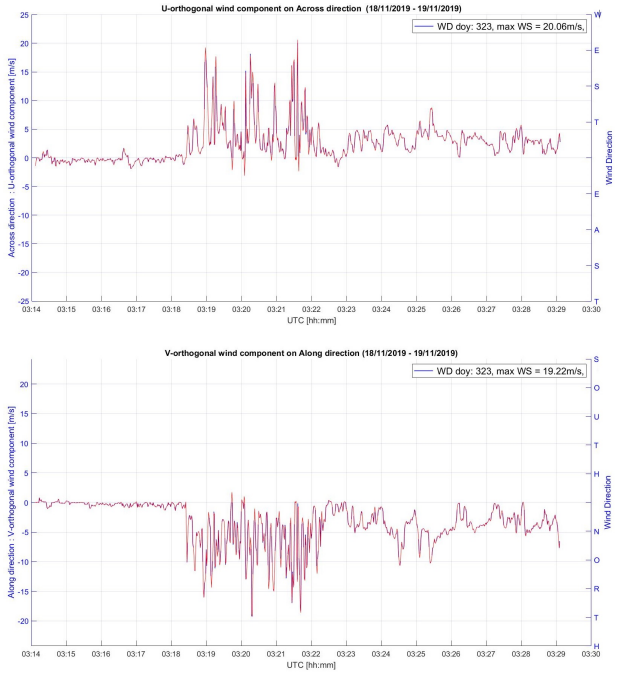

Figure 49. *across*$_U$ (top) and *along*$_V$ (below) orthogonal wind components against UTC time during 03:14:43 - 03:29:43, day 323. Right axes indicating correct WD (wind barf convention)

[43] the WS threshold value of 18 $\frac{m}{s}$ represented 75% of the maximal WS value from the studied time interval.

In the next step, their UTC time values were converted to their corresponding GPST values by adding 37 seconds. This correction factor corresponds to the amount of lag shift of windy day 323 with respect to the origin day 320 of 19 seconds plus the 18 leap seconds added to the UTC time from the beginning of GPST time frame. The resulting GPST values were marked with black dots in Figure 50 and were used for highlighting the across/ along wind-induced deformation values that were corresponding to West winds with WS values $\geq$ than 18 $\frac{m}{s}$.
One should know that the mean and root mean square error values from the legends of Figure 50 were computed based on the *across/ along*$_{WND_{323}}$ values within the time interval of interest. From the numbers presented in the legends of Figure 50, one can conclude that the building moved on average 0.32 mm to the West and 0.32 mm to the North under the influence of several seconds when West winds blew with speeds $\geq$ than 19 $\frac{m}{s}$.

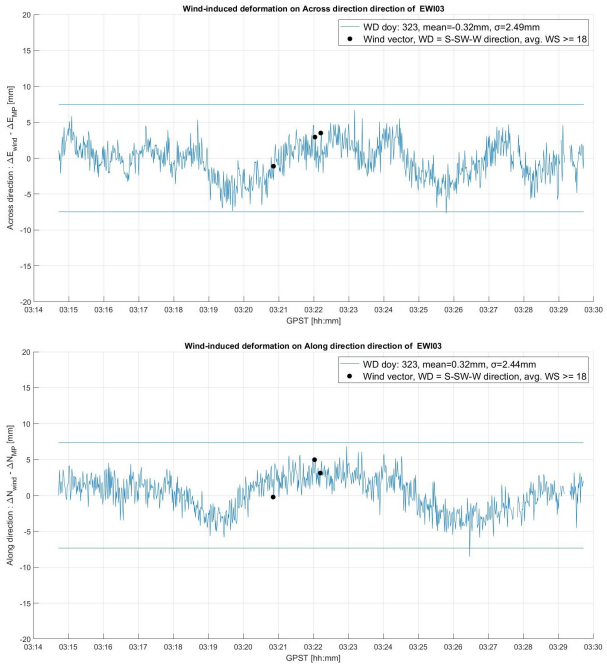

Figure 50. across/ along$_{WND_{323}}$ time series vs GPST during 03:14:43 - 03:29:43, day 323. Black dots correspond to powerful wind activity blowing from favorable cardinal direction which should produce building deflections.

Since the across wind-induced deformation time series from the upper part of Figure 50 started to peak in across direction immediately after the appearance of the first black dots, one could conclude that the black dots matched better with the displacement behavior within the *across*$_{WND_{323}}$ time series than within the *along*$_{WND_{323}}$ time series. These findings are in accordance with the expected structural behavior of the building. Knowing that the three dots corresponded to West wind stresses (see Figure 48) they should normally not produce significant displacements in along direction.

Even when visually searching for correlation between across/ along wind-induced deformation time series and WS time series of day 323 one could identify remarkable similar patters between the *across*$_{WND_{323}}$ and the WS time series. In order to visualize this, the first three big peaks in the WS time series plot (see top plot from Figure 51) were grouped and marked with red while the next, half as large, WS peaks were grouped and marked with yellow. The exact same pattern could be found in the *across*$_{WND_{323}}$ time series (see middle plot from Figure 51). Partly the same pattern could be found in the *along*$_{WND_{323}}$ time series (see below plot from Figure 51) as well.

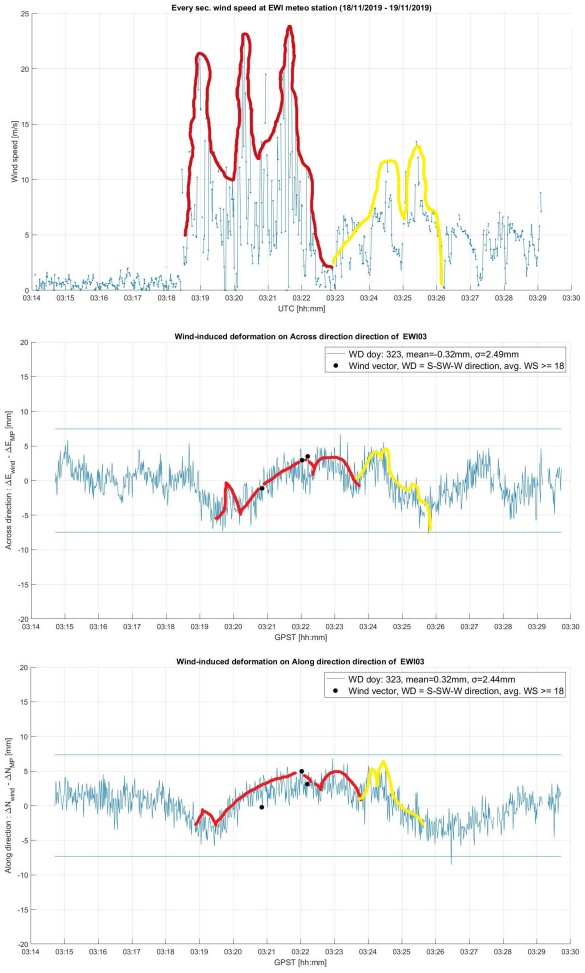

Figure 51. Remarkable strong visual correlation between WS measurements and *across/ along*$_{WND_{323}}$ coordinates during 03:14:43 - 03:29:43, day 323. Note that for day 323 there is a 37 sec. lag shift between UTC and GPST time frames

In case of windy day 331 a 21 minutes time interval spanning from 11:18:23 to 11:39:16 UTC was chosen. This specific time stamp captured the highest WS values of day 331. Some of the time instances corresponded to samples of powerful winds that were blowing from South, South-West or West direction and/ or from North, North-East or East direction. But when carefully inspecting plot **b** from Figure 45 one identified that during that time period the wind was blowing on average from South-East direction perpendicular to one of the concrete walls of EWI. This was verified by visually inspecting the right axes of Figure 53.
Nevertheless, on this specific time span the same Matlab script mentioned above was used in order to ask for the time instants of South, South-West or West and/ or North, North-East or East winds that were hitting the glass walls of EWI perpendicularly. Thirty-three instants were found in accordance with these conditions. Twenty-six of them were corresponding to South,

South-West or West winds with magnitude $\geq$ than 19 $\frac{m}{s}$ while the remaining were corresponding to North, North-East or East winds with magnitude $\geq$ than 19 $\frac{m}{s}$ (see Figure 52). The WS threshold value of 19 $\frac{m}{s}$ was computed as presented before for day 323.

S-SW-W direction meas.			
UTC	WD	WS	Cardinal dir.
11:21:50	178	23.6	S
11:22:41	180	22	S
11:24:32	200	22.9	SSW
11:24:37	181	22.5	S
11:25:07	178	24.7	S
11:25:08	171	21	S
11:25:12	182	24.9	S
11:26:08	180	24.3	S
11:26:11	185	24.6	S
11:26:15	195	20.7	SSW
11:26:16	199	19.4	SSW
11:26:31	183	24.5	S
11:26:40	208	19.3	SSW
11:28:26	180	24	S
11:28:27	190	25.1	S
11:28:32	173	20.6	S
11:28:37	194	21.4	SSW
11:28:56	197	19.6	SSW
11:29:31	174	22.3	S
11:29:36	177	24	S
11:30:01	187	23.2	S
11:30:29	192	23.4	SSW
11:30:30	183	20.2	S
11:30:33	191	23.7	SSW
11:30:35	170	23.7	S
11:30:39	175	20.6	S

N-NE-E direction meas.			
UTC	WD	WS	Cardinal dir.
11:22:05	95	20.5	E
11:33:41	65	19.9	NEE
11:34:30	98	23.9	E
11:34:48	90	19.3	E
11:35:17	94	21.5	E
11:35:29	92	24	E
11:35:32	94	19.7	E

Figure 52. S-SW-W (left) and N-NE-E (right) WD, WS measurements and cardinal direction inventory during 11:16:40 - 11:37:33, day 331

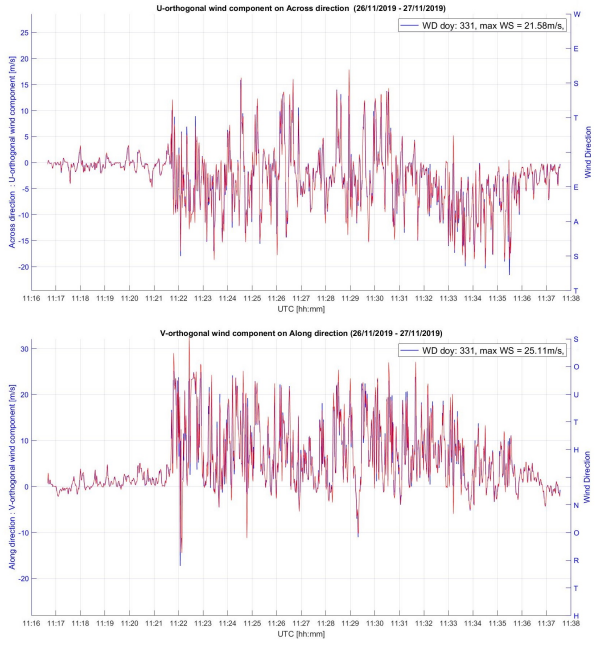

Figure 53. $across_U$ (top) and $along_V$ (below) orthogonal wind components against UTC time during 11:16:40 - 11:37:33, day 331. Right axes indicating correct WD (wind barf convention)

As a side note, while manually inspecting the WD values in the proximity of the studied time span, unexpected WD changes of powerful winds were found. Figure 54 shows how the wind changed its direction within 9 seconds many times, from South-East to North then to East and finally settling back to North direction. Such drastic WD changes can happen under light winds but in this case they happened under strong winds. This makes one rise a question about the integrity of the acquired meteorological data sets during powerful wind storms.

UTC	WD	WS	Cardinal dir.
11:21:59	134	12.6	SE
11:22:00	145	24.2	SE
11:22:01	180	7.1	S
00-Jan-0000 00:00:00	NaN	NaN	NaN
11:22:03	134	16.6	SE
11:22:04	0	18.9	N
11:22:05	95	20.5	E
00-Jan-0000 00:00:00	NaN	NaN	NaN
11:22:07	308	12.7	NW
11:22:08	0	14.8	N

Figure 54. Rapid change in WD during wind storm. The acquired WD values might fluctuate because of acquisition errors of the meteorological station

In the next step, the UTC time values of the selected time stamps were converted to their corresponding GPST values by adding 103 seconds to them. This correction factor corresponded to the amount of lag shift of windy day 331 with respect to the origin day 320 of 85 seconds plus the 18 leap seconds added to the UTC time from the beginning of GPST time frame. The resulting GPST values were marked with black/ red dots in Figure 55 and were used for highlighting the:

- $across_{WND_{331}}$ values that were corresponding to South, South-West or West winds with WS values $\geq$ 19 $\frac{m}{s}$ $\rightarrow$highlighted with black dots
- $along_{WND_{331}}$ values that were corresponding to North, North-East or East winds with WS values $\geq$ 19 $\frac{m}{s}$ $\rightarrow$highlighted with red dots

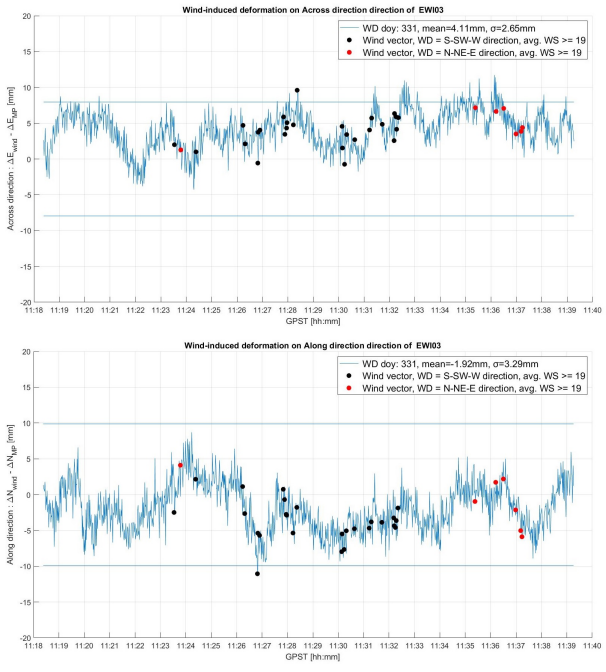

Figure 55. $across/along_{WND_{331}}$ time series vs GPST during 11:16:40 - 11:37:33, day 331. Black and red dots correspond to powerful wind activity blowing from favorable cardinal direction which should produce building deflections

The mean and root mean square error values presented in the legends of Figure 55 are computed based on the across/ along wind-induced deformation values ($across/\ along_{WND_{331}}$) within the time interval of interest during day 331. From the numbers presented in the legends of Figure 55 one can conclude that during the time span of interest the building moved on average 4.11 mm to the East and 1.92 mm to the South, under the influence of several seconds when South-West and/ or North-East winds blew with speeds $\geq$ than 19 $\frac{m}{s}$.
From the top plot of Figure 55 one can clearly identify that most of the East oriented peaks which were exceeding the 3σ threshold appeared immediately after and sometimes at the same time with the black dots. In addition, the last part of the top plot shows how the deflection direction changed from East to West direction right after the appearance of the red dots.
In the lower plot of the same figure the influence of South-West winds on the $along_{WND_{331}}$ position time series was smaller since only one peak, exceeding the 3σ threshold, could be identified. In this plot most of the wind measurements were correlating with the expected displacement behavior but there were some suspicious black dots that described an unexpected South displacement of the building during South wind stresses. This can be identified under the form of a V-pattern in the middle part of the lower plot. In addition, the winds corresponding to the last red dots should have had a small influence on the building displacement since most of these wind measurements were coming from East direction (see Figure 54) but from this plot one gets the impression that they had a big influence by moving the building 1 centimetre from North to South direction.

In case of day 331 a poor visual correlation between across/ along wind-induced deformation time series and WS time series was identified. In Figure 56 both displacement time series described the same pattern which partially followed the noisy WS pattern.

In conclusion, since the proposed procedure for identifying possible wind-induced displacements by searching for statistical normalized cross correlation, over full sidereal days with intense wind activity, between $across_{WND}$ and $across_U$ time series and between $along_{WND}$ and $along_V$ time series was not satisfactory, one was needed to zoom in the across and along wind-induced displacement time series and search for ideal cases when strong wind was blowing from South-West and/ or North-East direction, perpendicular to the glass façades of EWI. On behalf of two studied time intervals over days 323 and 331, one was able to identify starting points of possible wind-induced displacements in the across/ along wind-induced deformation time series of both windy days. These were marked with black and red dots in the previous created plots. Most of these values were in accordance with the expected structural behavior of the EWI building under favorable wind stresses. In addition, for day 323 one could even find visual similarities between the $across/\ along_{WND_{323}}$ patterns and the WS data set (see Figure 51).
Despite, one could still argue if what the previous plots showed could be related to building displacements caused by 6 Beaufort wind stresses that were in their early stage of formation or it could be related to remaining MP effect within the across/ along wind-induced deformation time series. When summarizing all findings from this chapter a rational answer to the second research question would read that: under the influence of presented meteorological conditions one cannot be sure about the capabilities of the used low-cost dual frequency

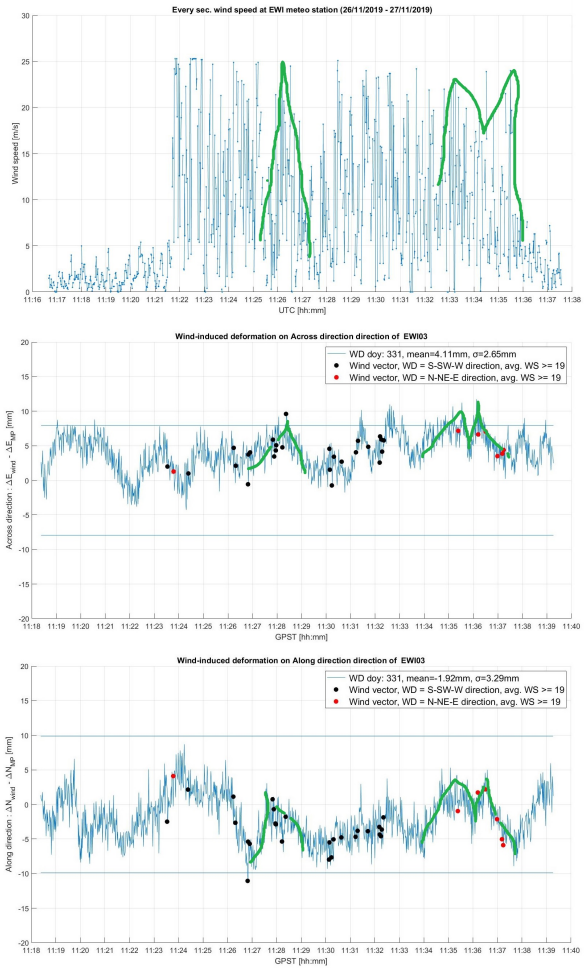

Figure 56. Vet poor visual correlation between WS measurements and across/ along$_{WND_{323}}$ coordinates during 11:16:40 - 11:37:33, day 331. Note that for day 331 there is a 103 sec. lag shift between UTC and GPST time frames

GNSS modules to identifying wind-induced displacements in EWI's structure. On the other hand, this equipment might be sufficiently accurate for retaining building displacements if these are larger than the inferred MP effect on carrier phase observations. This scenario can happen under more powerful and long-lasting wind storms that should blow on average from South-West and/ or North-East direction.

7. RESULTS DISCUSSION & CONCLUSIONS

7.1 Summary of findings

In this subsection prompt answers to the phrased research questions based on the previously discussed results are formulated. Their main goal was to guide for achieving the final research objective of designing and applying a low-cost GNSS building deformation study in order to test the actual accuracy capabilities of the newly released low-cost dual frequency GNSS modules to sense structural wind influences on the EWI building by establishing an optimal network emplacement of GNSS receivers, acquiring dual frequency code and carrier phase observations and computing relative horizontal positions and accuracy estimates based only on carrier phase data subject to many corrections.

As it was presented, this research project was set on a 90 metres tall concrete-steel structure, EWI building, where four low-cost dual frequency GNSS modules were installed over twenty days to acquire high-frequent code and carrier phase observations. The later observations were analyzed in order to sense possible wind-induced displacements of this building. Under the assumption that the building would be influenced by a 8 Beaufort wind gale, perpendicular to the glass sides of the building, 1.3 centimetre deflections were expected (see chapter 3).

Based on the first PPK processing results presented in this paper one can attest that the used low-cost dual frequency GNSS modules are capable to output relative position estimates with millimetre precision under any meteorological conditions. The legends from Figure 28 prove this by indicating root mean square errors of up to approximately 5 millimetres on East and 7 millimetres on North direction during the studied wind-still days 320, 321 and 324. In order to make the equipment output such accurate position results, one needed to filter out all unwanted solutions by using a two-step filtration procedure presented in the middle part of subsection 5.3. Slightly poorer results were registered during windy days influenced by short periods of 6 Beaufort winds and 8 $\frac{mm}{h}$ rain (see legends from Figure 30 and 31). But after further correcting for "leaking" MP effects, by using the GPS sidereal repeatability technique (see subsection 5.3 and 5.5) in order to define a MP pattern and subtract it from any windy day relative position time series, one obtained small root mean square error values of maximum 5 millimetres as well (see legends from Figure 32 and 33). The price to pay was related to noise increase in the resulting relative position time series of both chosen windy days, 323 and 331.
All in all, throughout this study a low-cost dual frequency GNSS module offered millimetre accurate position solutions, proving that it can be a challenging competitor to high-end but more expensive geodetic GNSS receiver.

On behalf of the results from the conducted structural health monitoring case study, one cannot be sure about the capability of the used dual frequency GNSS modules to identify wind-induced displacements in EWI's structure. This conclusion is attested by the results from the previous subsection showing very poor correlation between wind-induced displacement time series and wind measurements time series of the two most windy days, 323 and 331.
In addition to the discussion from the previous subsection on the results of the wind-induced displacement analysis, a list of possible explanatory factors, justifying why the used GNSS module could not sense any convincing wind-induced displacements, is presented below:

- **Too weak and short windstorms over the study period**
  Short periods of 6 Beaufort wind breezes were detected during day 323 and 331. On behalf of the conservative deformation hypothesis discussed in chapter 3, a 6 Beaufort wind breeze would produce building displacements smaller than 1.3 centimetres. Such small displacements are hard to be captured under MP errors of minimum 1.5 centimetres[44]even after mitigating part of it.
  For example, from Figure 50 and 55 one could conclude that the relative position patterns are describing an up and down motion which is very similar to the sinusoidal behaviour of MP. Therefore, it is still debatable if the behaviour in the *across/ along*$_{WND_{323/331}}$ time series were indeed wind-induced deflections in their early stage of formation or it was just remaining MP effect within the relative position time series.

- **Too rigid case study building**
  Chapter 3 characterizes the EWI building from a structural point of view. There it was described that the building is consisting of two sides built of stiff concrete (South-East and North-West façades highlighted in blue in Figure 1), making this building not ideal for conducting a structural health monitoring campaign for measuring possible wind-induced displacements within its structure. In addition to this, professor M. Veljkovic was doubtful about identifying any wind-induced displacements of such a complex structure as EWI. He further, suggested to conduct a similar study on simpler steel structures for which precise and fully controlled displacement hypotheses could be defined.

- **Corrupted WD measurements**
  At one point while manually inspecting the WD measurements in the proximity of a windstorm event, unexpected WD changes were found. Figure 54 highlighted a 180 degrees WD change that was happening within a few seconds. Intriguing was that this happened under strong winds which is completely abnormal and physically impossible. Hence the integrity of the used meteorological data sets is arguable. It is very important to rely on valid meteorological data sets in order to aim for any statistical cross correlation between possible wind-induced deflections of the structure and wind behaviour.

On the other hand, subsection 6.1 demonstrated that the used low-cost dual frequency GNSS module was capable of retaining centimetre order permanent displacements of buildings without even correcting for MP effect. Although this outcome was artificially induced it proves that this type of GNSS equipment can be used for monitoring permanent displacements of tall buildings over long periods.

When taking these factors into account one could conclude that this equipment might be sufficient accurate for retaining building displacements, if these are larger than the magnitude of the "leaking" carrier phase MP effect.
In the case of the EWI building this scenario can happen under more powerful and long-lasting windstorms which should blow on average from South-West and/ or North-East direction perpendicular to its glass façades. In addition, one should be confident on the integrity of both GNSS and meteorological data sets when conducting such study.

7.2 Results impact & Future recommendations

Based on the previous presented results which were answering both main research questions of this study, the first steps in testing the capabilities of low-cost dual frequency GNSS equipment for monitoring large-scale building deformations were made. This study proves that low-cost dual frequency GNSS modules can offer millimetre position accuracies after applying several corrections. Moreover, it informs on

[44]this generic values was estimated based only on ground reflections from wet environments. For more details see first part of subsection 5.3.

the possibility of using them for sensing centimetre order displacements of large-scale buildings that are exceeding the magnitude of carrier phase MP effect.
Hence the newly released affordable dual frequency GNSS receivers can be seen as a linking bridge between high accuracy, acceptable expenses and low power consumption from which building process constructors, company owners and developing countries research institutes in search for sub-centimeter precise monitoring at cheap prices, can benefit.
In addition, this paper presents an effective way to mitigate the MP effect as well. This piece of knowledge is applicable to past research done in this field since this type of error is predominant when using affordable GNSS antennas for monitoring purposes.
Therefore, the presented findings about the accuracy limitations of these new "gadgets" are of great interest since they can validate past research on low-cost GNSS monitoring applications and provide more information about the technical and economical reliability of dual frequency low-cost GNSS receivers for determining large-scale building deformations and ensuring a safer environment.

Based on all insights from this paper, the author recommendations for further work include:

- **Better choice of the case study building**
  Choosing a more flexible and simpler case study building will facilitate full control over the deformation analysis and the definition of a displacement hypothesis. The case study building should be prone to wind-induced deflections. Hence it should be simpler and preferably built out of steel[45].
- **Better choice of the experimental setup**
  Choice of the installation emplacement of the used low-cost GNSS module network is crucial for getting high ambiguity fixing rates. Hence no line of sight occlusions are desirable. In addition, each receiver should be installed together with a ground plane for minimizing MP effect as much as possible.
- **High frequent data sets exploitation**
  Develop an algorithm that uses 10 Hz or at least 5 Hz GNSS data sets for identifying any building deflections and/ or vibrations. According to the Nyquist theorem this would give the possibility of identifying building vibrations of up to 5 respectively 2.5 Hz.
- **Influence of powerful and long-lasting wind storms**
  In order to validate the final conclusions of this study similar studies should be conducted where the case study building should be influenced by long-lasting 8 Beaufort or larger windstorms.
- **Validation of meteorological data sets**
  In case of further analysing meteorological data sets acquired by the EWI meteorological station, a validation of the integrity of these data sets with a different data set coming from another close-by meteorological station is needed.
- **Choice for windy days with zero-precipitation**
  By choosing windy days with no recorded precipitation it will help minimizing the MP effect since the surrounding environment would be dry.
- **Implementation of the lag shift correction in the created-sidereal day generation process presented in the last part of subsection 5.3**
- **Future real time monitoring system development**
  The presented knowledge can be possibly used for creation of real time monitoring systems based on low-cost GNSS equipment.

Summarizing all recommendations, it would be optimal to conduct a similar study on a *simpler* and/ or *more flexible steel structure*, such that one can verify the observed structural motion by means of models used in structural engineering using reliable wind-measurements as input, and develop an automatized algorithm based on the data processing steps listed in this study. These processing steps are summarized below in a step-by-step algorithm that can be used as well for reproducing the obtain results of this research project:

Step-by-step algorithm
In order to reproduce the results of this study the following algorithm can be applied on wind-still and windy 1 Hz GNSS data sets and meteorological data sets spanning over the case study period:

- PPK processing via RTKLib 2.4.3 based on the processing configurations from Figure 9 (see subsection 5.1)
- Meteorological data processing for identifying wind-still and windy days (see subsection 5.2)
- Cycle slips correction, completion with NaN values and creation of 86400 samples 1 Hz .pos files (see subsection 5.3)
- Created-sidereal day cuts (see subsection 5.3)
- Two-step filtration algorithm of poor and unwanted position solutions based on $3\hat{\sigma}$ criterion (see subsection 5.3)
- Lag shift correction (see subsection 5.3)
- Definition of MP pattern by overlapping wind-still days time series (see subsection 5.3)
- Two-step filtration algorithm on windy days time series (see subsection 5.4)
- Correction for MP effect. Definition of possible wind-induced deformation time series (see subsection 5.4)
- Coordinate system transformation of GNSS based relative position time series. From ETRF2000 DLF1 coordinate system to a local coordinate system (see subsection 5.5)
- Separation of wind measurements into U/ V orthogonal wind components. Rotation on same direction with local coordinate system of GNSS based relative position time series (see subsection 5.5)
- Wind-induced displacement analysis. Finding statistical cross correlation and/ or visual correlation (see chapter 6)

[45] recommendation from professor M. Veljkovic.

In such a case, one needs to make sure that the case study building will be affected by windstorms of at least 8 Beaufort. This automatized algorithm should exploit the capabilities of 10 Hz GNSS data sets to retain wind-induced displacements and further validate the conclusions drawn in this study. In case of obtaining positive results the knowledge can be used to develop a real time monitoring system based on low-cost dual frequency GNSS equipment.
In future the body of knowledge related to structural health monitoring based on low-cost GNSS equipment is expected to enrich with the appearance of many studies on low-cost dual frequency GNSS applications. This will facilitate the appearance of low-cost GNSS based real time monitoring systems in need for ensuring a safe environment.

7.3 Critical reflection

This subsection was meant for critically reflecting on achieving the personal learning objectives of this research project.
Before starting this research project an extensive research plan[46] was proposed and discussed with the daily supervisor of the research project, C. Tiberius. In the proposal a list of the most intriguing research questions and the main research goal were presented. Two of these were picked as main research questions and were addressed in chapter 1. These had the aim to guide the researcher towards achieving the final goal of "designing and applying a low-cost GNSS building deformation study in order to test the actual accuracy capabilities of a newly released low-cost dual frequency GNSS module to sense structural wind influences on the EWI building by establishing an optimal network emplacement of GNSS receivers, acquiring dual frequency code and carrier phase observations and computing relative horizontal positions and accuracy estimates based only on carrier phase data subject to many corrections".
Answers to both questions were phrased based on the results of the wind-induced deformation analysis in chapter 7. Since the answer to the second research question could not be fully answered yet for various reasons, one can affirm that the final research goal of this project was not entirely achieved. But in addition, an extensive list of recommendations was presented. These should be followed when conducting future related research in order to validate the findings from this paper and fully achieve the main research goal.
On behalf of the literature review a to-be-followed methodology and experimental setup were proposed in the research plan. When analysing the proposed methodology, one first needed to choose for the deformation type of most interest, which in this case were possible horizontal displacements caused by 8 Beaufort wind reaching up to 1.3 centimetres (see chapter 3). In the next step the followed processing technique needed to be selected. Based on the final conclusions from the literature review, PPK relative positioning was chosen for this study. Indeed, the DLF1 station was used as base station for applying relative positioning. Moreover, for processing the acquired GNSS data sets RTKLib 2.4.3 package was used in accordance with the research proposal.
A first difference between the proposed GNSS network and the applied one was that in practice one only used four low-cost dual frequency GNSS receivers, instead of five, to acquire 10 Hz code and carrier phase double frequency measurements. At least three days were planed for the structural health monitoring campaign. This proved to be wrongly estimated since one needed to let the equipment measure over twenty days in order to be able to reach some 6 Beaufort short wind breezes. Sadly the capability of the 10 Hz GNSS data sets was not studied since one first needed to explore the capability of 1 Hz GNSS data sets to retain any wind-induced deflections. The acquired measurements were corrected for MP and cycle slips as proposed. But instead of using the proposed carrier phase double difference residuals method described in (de Bakker et al., 2009) one used the GPS repeatability property and a two-step filtration algorithm presented in subsection 5.3. No validation procedure was conducted but it should be taken into consideration for further studies. Accelerometer- or robotized total station based data sets can be used in order to validate the findings. Because of lack of time, no identification of periodic effects induced by wind to the building position through harmonic analysis or least squares harmonic estimation was conducted. This type of vibration analysis was taken into consideration for application only if time allowed.
Last but not least, all drawn conclusions from this paper were based on empirical accuracy values computed based on least squares estimation theory on behalf of which the relative position estimation was also based. In addition to what was proposed, statistical cross correlation and visual correlation between GNSS based relative position time series and wind time series were applied. Time series analysis on full days and on short periods of these days was performed in order to detect possible wind-induced horizontal displacements.

Since planning plays an important role when pursuing research, a Gannt chart was attached to the research proposal. This chart had the purpose of organizing the intended actions in order to achieve the research objective in time. Even though in most cases the allocated time period for each intended action suffered changes, it was very important to have a defined schedule containing all intended actions and milestones.
In the next lines the most important impressions on the actions that took more than expected were subjectively confessed. From my personal experience, it was very important to conduct several data acquisition tests before installing the GNSS equipment on the roof top of EWI building. Three tests were conducted in order to successfully set up the GNSS receivers to log 10 Hz data sets. These were done before the beginning of this research project and were not taken into account in the Gannt chart. Hence, it is recommended to take such tests into account before setting up a GNSS network for measuring wind-induced displacements. As said before, the measurement campaign took much longer then was expected. Twenty days were needed in order spot short 6 Beaufort wind stresses. Planning the duration of the measurement campaign was subjective and it depended on the meteorological conditions on site.
Both the correction of MP and cycle slips and the PPK processing campaigns took more time then was expected. In addition, one did not expected to have problems when processing 10 and 5 Hz GNSS data sets. But because it was time consuming to process them in batches and splice them together using a PC, TU Delft's HPC cluster server was used for PPK processing of these computational complex files (see last part of subsection 5.1). Therefore, its use is highly recommended in order to save precious time.
From all intended actions presented on the Gannt chart only the spectral domain analysis was not performed and should be taken into consideration for further research.
All in all, this research project gave me a lot of fulfilment by offering me the possibility to design my own research project, set up and conduct a geodetic measuring campaign and apply

[46] the research proposal was attached to this document.

most of the principles presented in the course "CIE4522 - GPS for Civil Engineering and Geosciences" by H. van der Marel, S. Verhagen and C. Tiberius. In addition to these, I needed to understand and deal with some terminology related to structural engineering discipline which can be considered a new experience. Although I could not spot concrete patterns within the GNSS based time series describing wind-induced deflections of the EWI building, I declare myself satisfied by achieving 80% of my proposed personal learning objectives listed in the project proposal and Gannt chart.

ACKNOWLEDGEMENTS

The author of this report would like to express his gratitude towards Dr. ir. C. Tiberius for daily supervising this research project and for constantly suggesting new ideas for implementation, to A. Krietemeijer for providing the used u-blox ZED F9P dual frequency GNSS modules and for instructing on how to set them up for logging at 10 Hz rate, to Dr. ir. H. van der Marel for providing useful Matlab scripts that were updated and used along this research project and for offering guidance on choosing the most optimal MP pattern determination technique, to ing. F. van der Zwan for giving the permission and advice on where to install GNSS equipment on the EWI roof top, to ing. R. van Puffelen for providing meteorological data sets acquired by EWI meteorological station and for giving advice on how the data set was processed by the EWI/ Electronic Instrumentation Laboratory, to H. Dun for giving instruction on how to set up a SSH connection with TU Delft's HPC cluster via PuTTY and on how to launch PPK processing jobs to the HPC super computers, to Dr. M. Veljkovic for giving advice on the structural engineering side of the project and for suggesting valuable recommendations for future research, to R. Eggermont for giving access on using short QoS service of the HPC cluster, to L. Blonk for sharing the original document (van Bruggen et al., 1963) describing the structural calculations of the wind deformation on the glass façades of EWI.

REFERENCES

Cina, A., Piras, M., 2015. Performance of low-cost GNSS receiver for landslides monitoring: test and results. *Geomatics, Natural Hazards and Risk, 2015. 6(5-7): p. 497-514.*

de Bakker, P., van der Marel, H., Tiberius, C.C.J.M., 2009. Geometry-free undifferenced, single and double differenced analysis of single frequency GPS, EGNOS and GIOVE-A/B measurements. *GPS Solutions, 13 (4), 2009. 13.*

Heunecke, O., 2011. Landslide Monitoring Using Low Cost GNSS Equipment – Experiences from Two Alpine Testing Sites. *Journal of Civil Engineering and Architecture, Aug. 2011. Volume 5(No. 8 (Serial No. 45)): p. pp. 661-669.*

Lepadatu, A., Tiberius, C., 2014. GPS for structural health monitoring - Case study on the Basarab overpass cable-stayed bridge. *Journal of Applied Geodesy, 2014. 8(1): p. 65-85.*

Takahashi, S. et al., 2017. Real-time monitoring for structure deformations using hand-held RTK-GNSS receivers on the wall. *International Conference on Indoor Positioning and Indoor Navigation, IPIN 2017. 2017.*

Tamura, Y. et al., 2002. Measurement of wind-induced response of buildings using RTK-GPS. *Journal of Wind Engineering and Industrial Aerodynamics 90(12-15): 1783-1793.*

Teunissen, P. et al., 2017. *Springer Handbook of Global Navigation Satellite Systems.*

van Bruggen, J., P., Sterkenburg, I., J., Drexhage, G., Bodon, A., 1963. Technische Hogeschool Delft Electrotechniek HOOGBOUW, Berekening Windbelasting op de Lange Gevels.

van der Marel, H., 2017. Double Back-flip Corner Reflector GNSS Antenna Test Result.

APPENDIX

Logsheets:

CAMP:

GPS Logsheet

EWI01

SITE NAME: EWI roof top SITE ID:

Monument Inscription:

Location: Delft, NL

Type of Monument: Provisory benchmark + GP

Operator(s): Alexandru Mihai Lapadat

Institution(s): TU DELFT

Receiver Type: U-blox ZED F9P 00B 02 (24)

Receiver P/N:

Receiver S/N:

Receiver ID: F1100001656

Firmware version:

Sampling Int.: 0.1 sec. Elev. Mask: °

Start Date: 12 Nov 2019 DOY 316

Start Time (UTC): 14:46

Stop Date: 02 Dec 2019 DOY 336

Stop Time (UTC): 12:12

Comments:

Start-Stop time for clearing SD cards

Stop: 15 Nov. 2019, 14:10 UTC
Start: 15 Nov. 2019, 14:48 UTC
Stop: 25 Nov. 2019, 12:24 UTC
Start: 25 Nov. 2019, 12:44 UTC

Antenna Type: ANN MB 00 00

Antenna P/N:

Antenna S/N:

Antenna ID: AGA 556022 SO A9

Alignment:

☐ Magnetic North
☐ True North

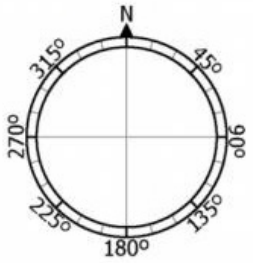

Magn. Decl.:

Comp. Reading:

Level: Start? Stop?

Centered: Start? Stop?

Height: Type: ☐ Vertical ☒ Slant

Read from: ☐ Bottom ☐ Top

Tripod: ☐

#	Start Height	Stop Height

Slant height in feet:

Average Slant Height: m

Corrected vertical height: m

☐ Spike Mount: Fixed Height: m

☐ Vertical Mount: Fixed Height: m

☐ Other: Height: m

CAMP:

GPS Logsheet

EWI02

Monument Drawing:

SITE NAME: EWI roof top SITE ID:

Monument Inscription:

Location: Delft, NL

Type of Monument: Provisory benchmark + GP

Operator(s): Alexandru Mihai Lapadat

Institution(s): TU DELFT

Receiver Type: U-blox ZED F9P 00B 02 (05)

Receiver P/N:

Receiver S/N:

Receiver ID: F1100001277

Firmware version:

Sampling Int.: 0.1 sec. Elev. Mask: °

Start Date: 12 Nov 2019 DOY 316

Start Time (UTC): 14:46

Stop Date: 02 Dec 2019 DOY 336

Stop Time (UTC): 12:12

Comments:

Start-Stop time for clearing SD cards

Stop: 15 Nov. 2019, 14:10 UTC
Start: 15 Nov. 2019, 14:48 UTC
Stop: 25 Nov. 2019, 12:24 UTC
Start: 25 Nov. 2019, 12:44 UTC

Artificial shift of 1.2 cm to East
on 25 Nov. 2019, 12:14 UTC

Antenna Type: ANN MB 00 00

Antenna P/N:

Antenna S/N:

Antenna ID: AGA 556022 SO A9 (4)

Alignment:

☐ Magnetic North
☐ True North

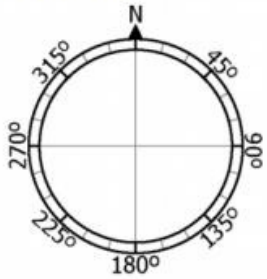

Magn. Decl.:

Comp. Reading:

Level: Start? Stop?

Centered: Start? Stop?

Height: Type: ☐ Vertical ☐ Slant

Read from: ☐ Bottom ☐ Top

Tripod: ☐

#	Start Height	Stop Height

Slant height in feet:

Average Slant Height: m

Corrected vertical height: m

☐ Spike Mount: Fixed Height: m

☐ Vertical Mount: Fixed Height: m

☐ Other: Height: m

CAMP:

EWI03

GPS Logsheet

Monument Drawing:

SITE NAME: EWI roof top SITE ID:

Monument Inscription:

Location: Delft, NL

Type of Monument: Provisory benchmark + GP

Operator(s): Alexandru Mihai Lapadat

Institution(s): TU DELFT

Receiver Type: U-blox ZED F9P 00B 02 (05)

Receiver P/N:

Receiver S/N:

Receiver ID: F1100001757

Firmware version:

Sampling Int.: 0.1 sec. Elev. Mask: °

Start Date: 12 Nov 2019 DOY 316

Start Time (UTC): 15:38

Stop Date: 02 Dec 2019 DOY 336

Stop Time (UTC): 12:20

Comments:

Start-Stop time for clearing SD cards

Stop: 15 Nov. 2019, 14:51 UTC
Start: 15 Nov. 2019, 15:01 UTC
Stop: 25 Nov. 2019, 12:12 UTC
Start: 25 Nov. 2019, 12:31 UTC

Antenna Type: ANN MB 00 00

Antenna P/N:

Antenna S/N:

Antenna ID: AGA 556022 SO A9 (3)

Alignment:

☐ Magnetic North
☐ True North

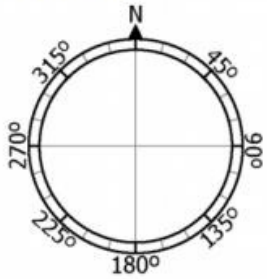

Magn. Decl.:

Comp. Reading:

Level: Start? Stop?

Centered: Start? Stop?

Height: Type: ☐ Vertical ☐ Slant

Read from: ☐ Bottom ☐ Top

Tripod: ☐

#	Start Height	Stop Height

Slant height in feet:

Average Slant Height: m

Corrected vertical height: m

☐ Spike Mount: Fixed Height: m

☐ Vertical Mount: Fixed Height: m

☐ Other: Height: m

CAMP:

EWI04

GPS Logsheet

Monument Drawing:

SITE NAME: EWI roof top SITE ID:

Monument Inscription:

Location: Delft, NL

Type of Monument: Provisory benchmark

Operator(s): Alexandru Mihai Lapadat

Institution(s): TU DELFT

Receiver Type: U-blox ZED F9P 00B 02 (10)

Receiver P/N:

Receiver S/N:

Receiver ID: F1100001570

Firmware version:

Sampling Int.: 0.1 sec. Elev. Mask: °

Start Date: 12 Nov 2019 DOY 316

Start Time (UTC): 15:38

Stop Date: 02 Dec 2019 DOY 336

Stop Time (UTC): 12:20

Comments:

Start-Stop time for clearing SD cards

Stop: 15 Nov. 2019, 14:51 UTC
Start: 15 Nov. 2019, 15:01 UTC
Stop: 25 Nov. 2019, 12:12 UTC
Start: 25 Nov. 2019, 12:31 UTC

Antenna Type: ANN MB 00 00

Antenna P/N:

Antenna S/N:

Antenna ID:

Alignment:

☐ Magnetic North
☐ True North

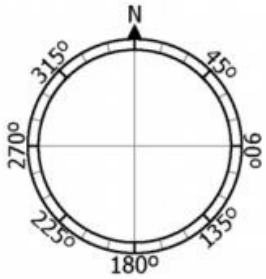

Magn. Decl.:

Comp. Reading:

Level: Start? Stop?

Centered: Start? Stop?

Height: Type: ☐ Vertical ☐ Slant

Read from: ☐ Bottom ☐ Top

Tripod: ☐

#	Start Height	Stop Height

Slant height in feet:

Average Slant Height: m

Corrected vertical height: m

☐ Spike Mount: Fixed Height: m

☐ Vertical Mount: Fixed Height: m

☐ Other: Height: m